VRIJE
UNIVERSITEIT
BRUSSEL

THE CMS TRACKER AS AN ADVANCED LEVER TO BOOST THE SEARCH FOR SEXAQUARKS

Thesis submitted in order to obtain the degree of master in Physics and Astronomy

Brent Danau

August 2023

Promotor: prof. dr. Steven Lowette

sciences and bioengineering sciences

Abstract

This Master thesis is a further study of the discovery potential of the theorized stable six-quark state that is strongly bound, also referred to as the Sexaquark, at the CMS. This particle was proposed by G. Farrar [1] and is to this day still a possible candidate for dark matter that is described by the Standard Model of particle physics.

The research in this study is largely based on the work done by J. De Clerq in [2], where a first-ever search strategy for the Sexaquark at the LHC was discussed. and builds further on his research. The Sexaquark particles could interact with the neutrons within the materials of the CMS detector, creating kaons and anti-lambda baryons, that in turn decay into pions and antiprotons. In the study performed by J. De Clercq, an upper limit was placed on the anti-Sexaquark production cross-section multiplied by the cross-section for the anti-Sexaquark annihilation with a neutron that results in a kaon and anti-lambda baryon. This upper limit was placed with the use of, among other things, reconstruction efficiencies and background cuts found in signal simulations, in which the Sexaquarks could interact only in the beampipe of the CMS.

This thesis focuses on investigating the reconstruction efficiencies and background cuts in the scenario where a selected amount of additional material inside the CMS detector was considered in the signal simulation. Using these, a new improved estimate on the upper limit for the signal can be found.

Acknowledgement

First and foremost, I would like to thank my promotor and thesis advisor Prof. Dr. Steven Lowette of the Vrije Universiteit Brussel. There wasn't any moment throughout the year when Prof. Lowette's door wasn't open for any questions I would have. He consistently provided me with excellent guidance whenever I needed it, whether it was writing or research. I am very grateful to him for giving me this opportunity to work on this very interesting topic. Prof. Lowette generously gave me a lot of his time for this thesis. I would not have been able to do this without him.

With equal gratitude, I would also very much like to thank Wren Vetens (PhD student at the University of Wisconsin-Madison), for giving me interesting and insightful suggestions and help throughout the year. This thesis would not have been what it is without all the guidance she gave me during all the Zoom meetings.

Contents

1   Introduction

The Standard Model of particle physics has been a huge success over the past decades, but it still fails to answer some of the big open questions in modern-day physics. One of these is the existence of Dark Matter, a weakly interacting particle that makes up about a quarter of the energy density of our Universe. In section 2, some observational evidence for this Dark Matter will be discussed, as well as the possible search strategies for it.

The existence of hadrons, i.e. particles that consist of three quarks, as well as particles that are made out of two quarks, has been well established. These kinds of particles are also described by the Standard Model. However, the existence of exotic hadrons, which are particles that consist of more than three quarks, has only been first discovered in 2003, when the first four-quark state particle was observed. Since then, several more four-quark state particles have been discovered as well as some five-quark state particles. The Sexaquark is a six-quark particle that is strongly bound and has been proposed by G. Farrar [1]. The existence of this particle has to this day not been observed yet. The particle could be a possible Dark Matter candidate if its mass is in the proper range. The history of exotic hadrons, the Sexaquark and its properties will be discussed in section 4.
It is suggested by G. Farrar. that these Sexaquark particles could be produced in proton-proton collisions in hadron colliders. An interesting candidate to search for this Sexaquark particle is the Large Hadron Collider (LHC), a large underground-based circular collider based in Geneve, due to its high luminosity. In section 3, the LHC will be discussed, and in more detail the Compact Muon Solenoid (CMS), which is one of the experiments located at the LHC. The design of the CMS detector will be discussed in detail.

A first-ever search channel for the Sexaquark at the CMS was performed by J . De Clerq in [2]. Herein, signal simulations were used to determine the reconstruction efficiencies and background cuts efficiencies in the search signal in order to place an upper limit on the production of the $\bar{S}$ in the proton-proton collisions at the CMS. In this thesis, a study will be done for the same search channel of the Sexaquark at the CMS. However, in this research, an additional selected amount of detector material will be included in the signal simulation, compared to [2] where only beampipe material was included. We will focus on the kinematics of the particles involved in the search signal in the signal simulation of CMS, the reconstruction efficiencies, and background cuts efficiencies found in the signal simulation in order to reevaluate the upper limit placed in [2]. The signal simulation will be discussed in section 5, followed by the found reconstruction efficiencies in section 6, than backgrounds cuts are shortly studied in section 7, and finally a conclusion is given in section 8.

2 Dark matter

Dark Matter has been one of the main mysteries in Physics during the last century. Its existence is heavily indicated by astrophysical and cosmological observations. Through these observations, it is expected that Dark Matter is electrically neutral, stable, uncoloured, and weakly interacting. Measurements show that, in the standard Lambda-CDM model of cosmology, the energy content of our Universe is made up of about 26.8% dark matter. Despite the indirect observations, the exact nature of DM is not yet known and it has still not been directly observed. The standard model (SM) of particle physics fails to explain Dark Matter and its properties.

2.1 Observational evidence for Dark Matter

In general, the earliest evidence for dark matter came from the observation of luminous objects that, if they were only gravitationally affected by other luminous objects, moved faster than was expected. On galactic scales, important evidence for dark matter comes from the rotation curves of galaxies (in particular spiral galaxies), i.e. the rotational velocities of astronomical objects such as stars as a function of the distance from the galactic center.

Most of the luminous matter in a spiral galaxy sits in the disc and the budge. Circular velocities in Newtonian dynamics are given by

$$v(r) = \sqrt{\frac{GM(r)}{r}}, \tag{1}$$

with $G = 6.6743 \cdot 10^{-11} m^3 kg^{-1} s^{-2}$ the gravitational constant , r the radius and $M(r) = 4\pi \int \rho(r) r^2 dr$, with $\rho(r)$ the mass density, the mass contained in a radius r. Due to the fact that the disc fades away far from the center of the galaxy, it is expected that the mass $M(r)$ becomes constant at large r and thus that the velocity would decrease as $v(r) \propto r^{-1/2}$. However, for most of the spiral galaxies, a rotational velocity that is constant with the radius is observed. an Example is given in Figure 1 . In this Figure, it is clear that the rotational velocity becomes approximately constant after a certain radius. Assuming Newton's gravitation law, this thus implies the existence of a halo of non-luminous matter with a mass distribution $M(r) \propto r$ throughout the galaxy [3].
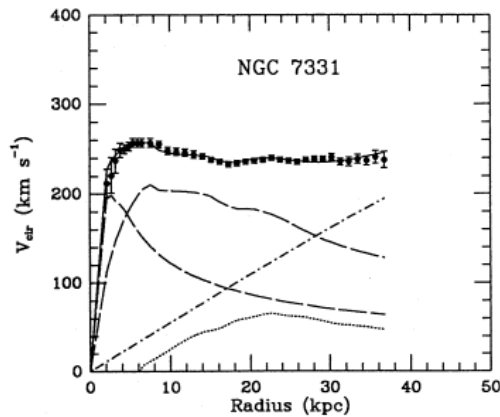
Figure 1: Rotation curve of NGC 7331. The contributions of disk, gas, and dark matter are given by the dashed, dotted, and dash-dotted lines, respectively. [4]

On a larger scale, other evidence for dark matter comes from the study of the mass-to-light ratio of galaxy clusters. The first hint for dark matter comes from observations on this scale, dedicated to F. Zwicky [5]. He found this first hint by measuring the velocity dispersion of the galaxies in the Coma Cluster and used this to infer a mass-to-light ratio of about 400 solar masses per unit of solar luminosity. This meant that the ratio in the solar neighbourhood was exceeded by two orders of magnitude.

Galaxy Clusters are large structures which consists of a large amount of galaxies gravitationally bound. A huge amount of gases are contained in these clusters in the interstellar medium and can reach very high velocities via acceleration by gravity and emit x-ray through thermal brehmsstrahlung. Analysis of these X-ray measurements can serve as a method to determine the mass of clusters. Other methods can be used to this purpose, including weak gravitational lensing, observing the distribution of the radial velocities in the cluster and applying the virial theorem.

A wonderful example for an indication of dark matter found through analysis of the X-ray measurements and gravitational lensing is that of Ref [6] for the Bullet Cluster 1E0657-558 and gives a finer understanding of the nature of dark matter. Fig 2 shows the image of this cluster. The blue region on this figure corresponds to the major part of the mass for the cluster found through gravitational lensing, while the red region corresponds to the hot gas observed through X-ray measurements. The Bullet cluster consists of two colliding galaxy clusters which can be revealed from the observed shapes in the figure. The right red zone corresponds to a smaller cluster which passed through the larger cluster on the left. The smaller cluster shows a shockwave form (bullet) which it received by passing through the larger larger cluster. This mismatch between the observed hot gas and the mass distribution found by gravitational lensing can be explained through the existence of dark matter. The hot gas experienced electromagnetic interactions throughout the collision which caused a drag force. However, the dark matter was not affected by this and thus did not experience this drag force, causing it to travel faster and further than the hot gas.
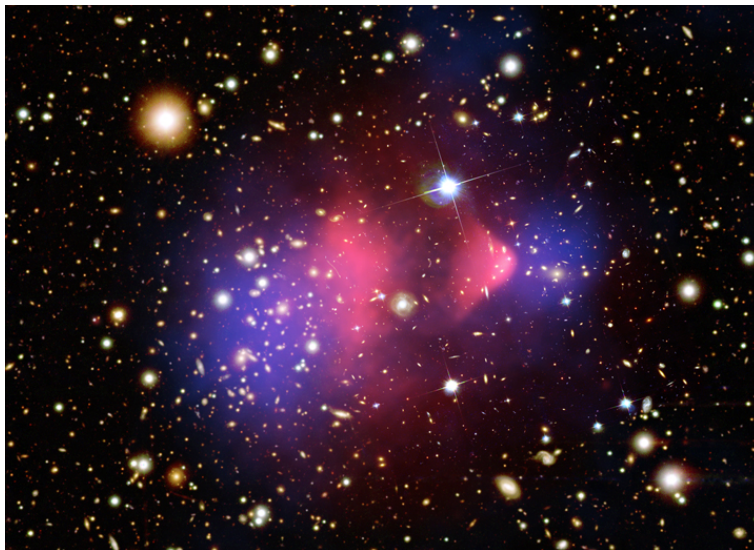
Figure 2: Composite image of Bullet cluster. Credit: NASA/CXC/CfA/M. Markevitch et al.; NASA/STScI; Magellan/U.Arizona/D. Clowe et al.; NASA/STScI; ESO WFI.

Lastly, dark matter plays an important role on cosmological scales and evidence on this scale can be found through the Cosmic Microwave Background (CMB) and the existence of old galaxies at a redshift of $z \approx 10$ [7, 8]. The CMB is a cooled leftover radiation from the photon decoupling in the early universe and is one of the most compelling evidence for the Big Bang model. In the early Universe, photons were in thermal equilibrium with all different types of particles until the expansion of the Universe caused the energy density to drop below the energy threshold necessary for photons to ionize hydrogen, after which photons could move freely. These photons can today still be observed, although with lower energy due to the fact that the Universe expanded. The observations of the CMB show that the density fluctuations at $z \approx 1$ are very small. Density fluctuations grow only in the matter-dominated era and when dark matter is present, matter domination starts earlier, which could cause the density fluctuations to also start earlier. Thus the presence of dark matter could explain these early formed galaxies. Measurements from the CMB can also be used to determine certain cosmological parameters, including mass densities of different kinds of matter in the Universe, through an analysis of the CMB anisotropies. Using the WMAP data, the following mass densities for baryons and matter was found [9]:

$$\Omega_b h^2 = 0.024 \pm 0.001 \quad , \quad \Omega_M h^2 = 0.14 \pm 0.02. \tag{2}$$

2.2   Experimental searches for dark matter

There are many general techniques used these days for the searches of different kinds of dark matter such as WIMPs, MACHOS (Massive Astrophysical Compact Halo Objects), sterile neutrinos, etc. However, these techniques can be split up into three basic methods :

- **Indirect search techniques** : This technique is based on the fact that dark matter particles can interact with their anti-particle partner. This annihilation interaction could cause the production of detectable particles such as, neutrinos, antiprotons, γ-rays, and

positrons. The IceCube experiment for neutrinos is a well-known example of this.

- **Direct search techniques** : Dark matter candidates could possibly interact with Standard model particles and thus could interact with detectors while passing through it. The PandaX experiment is an example of this search technique, where the dark matter particles could cause nuclear recoil on Xenon gas in the detector, which delivers a detectable signal.

- **Production in particle colliders** : The particles produced by the collision of Standard Model particles in particle colliders could be dark matter particles. These particles could then be shown to be present by looking at the missing momentum calculated from the Standard model particles created in the collision.

3   The Compact Muon Solenoid experiment

3.1   The Large Hadron Collider

The Large Hadron Collider (LHC) is the largest and most powerful particle accelerator in the world and is located at the CERN complex at the France-Switzerland border near Geneva. It is installed in a circular tunnel with a circumference of 27 km and it consists out of superconducting magnets to focus the particles and keep them on their track and has accelerating structures to boost particles. These superconducting magnets are made out of coils of electric cable which are cooled down to a significant temperature of $-271.3°$C to operate in this superconducting state. The large tunnel contains two adjacent and parallel beampipes in which beams of protons or heavy ions travel in opposite directions.

These two beams have 4 intersection points around the LHC ring. Around these points, detectors are made to reconstruct the particles created in the high energy collision of these beams of protons. There are four experiments created at these intersection points, namely, the CMS (Compact Muon Solenoid) , ALICE, (A large Ion Collider Experiment) , LHCb (Large Hadron Collider beauty) and ATLAS (A Toroidal LHC ApparatuS). From these four experiments, ALICE and LHCb have more specific roles, with ALICE designed to study the quark-gluon plasma form and LHCb desgined to study the b quarks. The CMS and ATLAS are more general-purpose particle detectors and are credited with the discovery of the Higgs Boson. Figure 3 shows an illustration of the total CERN complex in which the geometry of the LHC ring can be seen, as well as the location of the four experiments at the intersection points and a lot more structures.
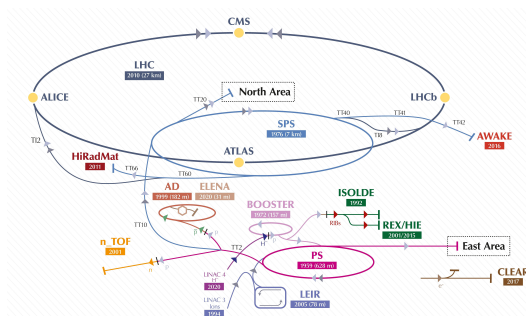

Figure 3: Illustration of the CERN accelerator complex [10].

3.2   The CMS design

The final state particles created, during the proton-proton beam collisions, at the LHC P5 intersection point at the LHC are measured there with the CMS detector. An illustration of the design of the CMS detector is shown in Figure 4. At the center of the design is the interaction point of the crossing beams, around which all the different sublayers of the detector are built. Particles created at this intersection point have the possibility to cross all these subdetectors found in the CMS. All of these subdetectors have their own specific purpose and are optimized for their own goals. Going radially, the most inner part of the detector is known as the pixel silicon tracker, followed by the strip silicon tracker, electromagnetic calorimeter (ECAL), hadron calorimeter (HCAL), and then finally the muon system.

In order to measure the momenta of the particles created in the collisions, a large magnetic field is needed as a bending force. Although the CMS has similar goals as the ATLAS experiment, different choices were made in this experiment for magnet-system design and technical solutions. For the CMS detector, a superconducting solenoid was chosen that is 13-m long, has a 5.4 m inner diameter, and creates a 3.8 T magnetic field. This quasi-uniform magnetic field causes the tracks of charged particles to bend, such that charged particles follow a helical path that can be described by five parameters. From these parameter values the momenta of the particles can be deduced from less than 100 MeV/c to more than $1 TeV/c$. Additionally, the charge of the particles can be found from the bending of the tracks as oppositely charged particles will bend in the opposite direction in the magnetic field. The inner tracking system, which is the group name for the pixel silicon and strip silicon tracker, and the ECAL are enclosed by this solenoid. Over the next sections, descriptions of each of the subdetector layers and their particle detection mechanisms will be discussed. Special attention will be given to the tracking detector as this will play a more important role further in this thesis.
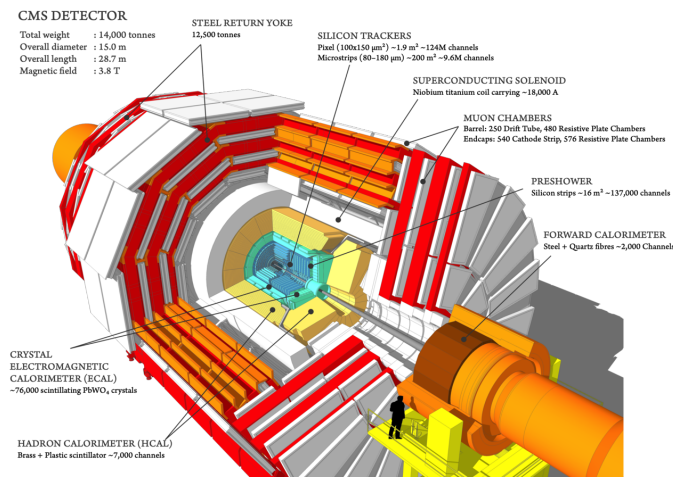

Figure 4: Diagram of the CMS detector design. [**?**]

3.2.1   The inner tracking system

The silicon pixel detector included in the CMS detector enables the reconstruction of trajectories and vertices of charged particles, by providing 3-dimensional space points of these particles within the 3.8 T magnetic field created by the solenoid. This inner tracking system is divided into two subdetectors, namely the pixel silicon tracker and the strip silicon tracker. Figure 5 gives a representation of the pixel silicon tracking systems for the Phase 0 design and the Phase 1 upgrade of the system in longitudinal view. These upgrades led to an improvement of tracking performances, lower mass, and the extra endcap disk provided a hit coverage up to an absolute value for pseudorapidity $|\eta| = 2.5$, with the pseudorapidity derived from the angle with the beamline axis as follows :

$$\eta = -ln \ (\ tan(\ \frac{\theta}{2} \ ) \ ). \tag{3}$$

The original CMS pixel detector, i.e. the Phase-0 detector, was replaced with an upgraded

version, i.e. the Phase-1 pixel system, during the year-end stop of the LHC in 2016/2017. The upgraded system was designed to cope with the higher luminosities achieved by the LHC after its upgrades in 2013/2014 and because the original detector already suffered damage due to radiation.
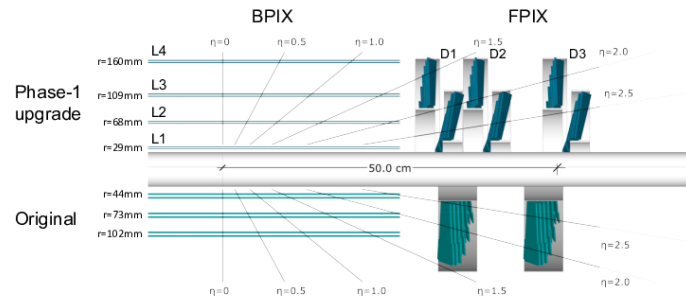

Figure 5: Layout of the Phase 1 pixel detector (top) compared to the Phase 0 pixel detector (bottom) in longitudinal view [12].

A division into subdetectors was made based on the particle flux at different radii for high luminosity. Pixel detectors are placed closest to the interaction points as the flux is highest on these radii and because pixel detectors give a lower occupancy per pixel per LHC crossing compared to the occupancy for the strips. In the Phase 0 pixel detector, the pixels had a size of $\approx 100 \times 150 \ \mu m^2$, which gave an occupancy of 10^{-4} per pixel per LHC crossing for particle flux of $\approx 10 \ \mu m^{-2} \ s^{-1}$ at a radius of $r \approx 10 \ cm$. The particle flux becomes low enough at intermediate regions of $20 \ cm < r < 55 \ cm$, such that strip detectors can be used with a minimum size of $10 cm \times 80 \ \mu m$, which leads to an occupancy of $\approx 2 - 3\%$ per LHC crossing. Finally, at even further regions, large silicon strips can be used with a size of $25 cm \times 180 \ \mu m$.

During the first long shutdown (LS1) of the LHC in 2013/2014, a beampipe with a smaller radius of $23 \ mm$, compared to the original one of $30 \ mm$, was placed in the CMS detector. This ensured a place for the innermost layer of the Phase-1 pixel detector, as can be seen from Figure 5. Furthermore, it can be seen that the upgraded system consists of three disks on each end, with distances of $291 \ cm$, $396 \ cm$, and $516 \ cm$, and of four concentric barrel layers, at distances of $29 \ mm$, $68 \ mm$, $109 \ mm$, and $160 \ mm$. The Phase-0 detector had a total silicon area of $\approx 1.1 \ m^2$, while the upgraded version now has a total silicon area of $1.9 \ m^2$.

As previously mentioned, the inner tracking system allows for a reconstruction of particle trajectories by using the 3-dimensional position measurements of the hits, i.e. the interaction points of the charged particles in the several layers of sensors, and connecting these hits. The actual CMS track reconstruction software is based on an extension of Kalman filters and produces the reconstructed tracks through a process called iterative tracking, where multiple iterations

of the tracking software are used. In the initial iterations, a search is made for the easiest-to-find tracks, such as for large transverse momentum or for ones that are produced with a small displacement. Then hits that are associated with the tracks are removed after each iteration, causing a simplification in the iterations so that lower transverse momentum and higher displacement tracks can be reconstructed in the later iterations. The process for each iteration can be split up into four steps, namely, seed generation, track finding, track fitting, and track selection. The procedures of the steps are as follows [13] :

- **Seed generation**: A track seed is the initial parameters settings for a trajectory and their associated uncertainties. The five parameters describing the path of the particles can be extracted from either two 3-D hits and a constraint on the origin of the trajectory or from three 3-D hits. Information about the locations of the primary vertices in the event and the position of the center of the beam spot is required for the generation of a seed. A fast track and vertex reconstruction algorithm is used for this, which uses only hits in the pixels. The extraction of a seed is controlled by two parameters, namely the seeding layers and the tracking region. The seeding layers are the pair or triplets of layers used to search for the hits. The tracking region is the constraints on the track parameters, e.g. minimum transverse momentum or maximum distance from a point. One hit per seeding layer is used to construct a seed. If the seeding layer consists of two layers, a pair of hits will be used to see if the track parameters corresponding to these hits fit the track region constraints. If the parameters are compatible with these, the seed is accepted.

- **Track finding** : The estimate for the track parameters found by the seed generation is used as an input for Kalman Filters which updates the parameter values as more hits from successive layers are added. This update for each hit at each different layer is performed with the knowledge of the hit position as well as the uncertainty on the position on the hit, the Coulomb scattering effects and energy loss in the detectors, and stochastic effects. The hit position and uncertainty values in a detector layer are refined using the track parameter values given by the Kalman filters at the previous layer and a selection of compatible hits is then made via a χ^2 test. The values keep on being updated with the information about the succeeding hits, until a stopping condition is met, e.g. reaching a tracker volume limit.

- **Track fitting** : After the track finding step, an estimate for the track parameters is found together with a collection of hits. However, it is possible for this estimate to be biased by certain constraints, e.g. beamspot constraint. For this reason, a Kalman filter is applied again on the track parameters during this step to get rid of these biases and so that inhomogeneities of the magnetic field and possible outlier hits are taken into account as well.

- **Track selection** : In a typical event, the first three track-finding steps described above, produce a number of reconstructed tracks that are not associated with particles. Quality requirements can reduce the number of these tracks. The criteria for these requirements are a minimum on the number of layers with hits for the track, limits on the track parameters values and a limit on the χ^2 of the track fit. These limits create a smaller, more pure collection of tracks.

3.3   The calorimeters

The purpose of the calorimeters is to measure the energy of particles passing through them. As previously mentioned, this information of the energy of the particle is measured by two differ-

ent kinds of calorimeter detectors in the CMS system, namely the electromagnetic calorimeter (ECAL) and the hadron calorimeter (HCAL).

The goal of the ECAL is to measure the energy of particles that interact through the electromagnetic force, such as electrons and photons, and also measures their position of incidence in the detector. The measurement of position allows for a possible distinction between single-incidence photons and closely created photon pairs that arise from the decay of neutral pions, also referred to as π^0-rejection. For the ECAL in the CMS system, a scintillation calorimeter was chosen because this offers a very good energy resolution, due to the fact that almost all of the energy of photons and electrons is deposited in the crystals. Scintillation is the process where photons or energetic particles, excite a material causing it to emit visible or UV light. More specifically, crystals of lead tungsten ($PbWO_4$) were chosen for the system. These crystals were chosen because they have a very high effective atomic number and a very high density of 8.3 g/cm^3, which causes a relatively small radiation length, i.e. the mean length into the material at which point the energy of an electron is reduced by a factor of $1/e$, of 0.89 cm. As a consequence, the crystals are relatively short, 23 cm in the barrel parts of the ECAL and 22 cm in the endcap parts, thus leading to a compact calorimeter. A total of 75848 crystals were used in the detector, where of 61200 in the barrel part and 14648 in the endcaps.

The interaction of the electrons and photons with the crystal creates scintillation light. The amount of this light is linear with the amount of energy of the particles. The light emitted by these crystals is measured by photodiode detectors that are placed nearby. The light creates an electrical signal in these detectors that is proportional to the amount of light and thus allows for an estimate of the energy of the particle.

The HCAL measures the energy and direction of jets, which are cones of hadrons and other particles that are produced through the process of hadronization, and the missing transverse energy of events, allowing for the identification and measurements of quarks, gluons, and neutrinos. Furthermore, the measurements of the missing energy can serve as a signature for new particles. The HCAL is subdivided into three parts, namely the forward HCAL, the barrel HCAL and the endcap HCAL. The barrel and endcap parts are calorimeters made out of thick brass plates that are interleaved with plastic scintillators. The incident hadrons create scintillation light in the form of violet-blue light, of which the amount is again proportional to the energy of the particles. The light is then transported out through optical fibers to Hybrid Photodiodes, in which an electrical signal is created.

The forward HCALs were placed such that the coverage of the detector reaches $\eta = 4.1$, meaning that these parts of the detector are in higher radiation zones. For this reason, these parts were made out of steel embedded with quartz fibers. As particles travel through the fibers, Cherenkov light is created. This light is measured and used to determine the energy of the jets.

3.4   The muon system

As the name suggests, the muon system's main role is the detection of muons. The CMS muon system is placed outside of the solenoid and consists of anode strip chambers in the forward regions and drift tubes in the barrel parts. The CMS drift tubes consist of tubes that contain gas and a stretched wire within the gas. As charged particles or muons travels through this gas volume, electrons will be knocked off atoms and the electrons will travel towards the cathode of the wire, where an electrical signal can be measured. The drift velocity of the electrons is an approximately constant value and thus by measuring the time it took for the electron the reach the wire in the tube, the exact location of the muon crossing through the tube can be found. The CMS drift tubes have a spatial resolution of 80 to 120 μm per chamber. The cathode

strip chambers are more complex but work through the same procedure where the particles will knock off electrons which will create an electric impulse. The spatial resolution of these is 40 to 150 μm. In the forward region, the muon rate is higher and thus faster detectors are needed in this region. This is the reason that cathode strip chambers are used in this region as the drift length for the electrons is smaller here compared to those of the drift tubes. Additionally, The CMS muon system also has resistive plate chambers in both the endcap and barrel regions. A representation of the CMS's muon system is shown in Figure 6.
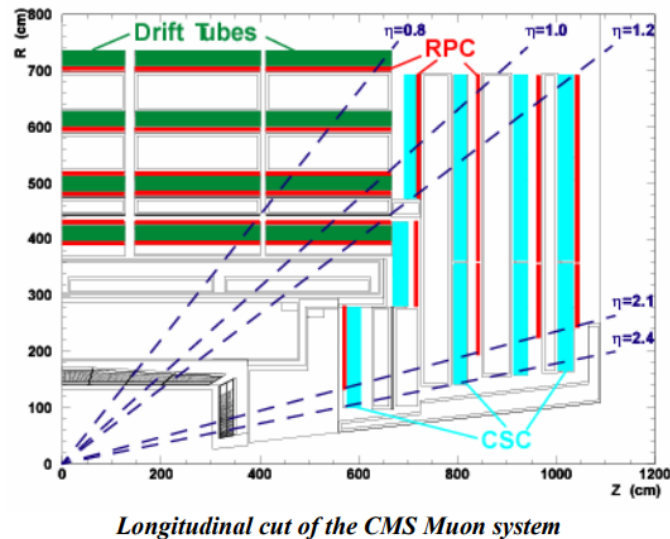

Figure 6: Layout of the muon system in longitudinal view. [14]

The barrel region consists of four different layers at increasing radii. These layers are made out of drift tubes, one or two resistive plate chambers, and are interleaved with return iron yoke. These iron yokes guide the return magnetic field outside the solenoid and allow for a good muon reconstruction while maintaining compactness for the detector.

3.5 The trigger and data acquisition system

The LHC bunch crossing rate of 40 MHz together with the LHC design luminosity of $10^{34}\ cm^{-2}\ s^{-1}$, results in a lot of data to be stored for the information about the interactions. About 1 Mbyte of data is created per bunch crossing. For the on-line computer to be able to store its maximum rate of data, the input rate of $40\ 10^{6}$ of bunch crossing per second has to be reduced to a rate of 100 Hz. CMS uses a two-level trigger system to reduce this rate, the level-1 trigger and the High-level trigger (HLT).

The level-1 trigger is a hardware trigger because it is based on custom electronics. A total time of $\approx 4\ \mu s$ is used to transmit the data and to make a decision whether to keep the data or not. While this decision is being made, the data is temporarily stored in buffers until trigger data is retrieved from the front-end electronics that discard a large fraction of the stored data. The trigger uses information from the calorimeters and muon system to determine whether events had interesting properties, e.g. muons, electrons, photons above a certain p_t involved. The system is made out of custom-designed microprocessors, such as ASICs, and programmable chips,

such as FPGAs.

The HLT analyses the full information from the subdetectors with the use of a computer farm of processors on which several software algorithms are used to further reduce the data, received from the level-1 system, from ≈ 100 kHz to ≈ 100 Hz. The selection of information for the HLT is then further transferred to the Tier-0 center of CERN, where the data is stored for a long time for reconstruction and data analysis.

4 The Sexaquark

Baryons are composite subatomic particles that consist of three valence quarks. Particles that are made out of a quark anti-quark pair are known as mesons. Both the baryons and mesons are part of the hadrons family of particles, which is simply the group name for particles that are made out of quarks. Most of the mass of the visible matter Universe is made out of the most known baryons, namely protons, and neutrons.

Quantum numbers are numbers that describe conserved quantities in a quantum system. An example of this is the Baryon number, which is defined as $B = \frac{1}{3}(n_q - n_{\bar{q}})$, with n_q the number of quarks and $n_{\bar{q}}$ the number of anti-quarks in the system. Obviously, this means that a quark has a baryon number of $B = \frac{1}{3}$ and baryons, containing three quarks, have a a baryon number of $B = 1$. There are more quantum numbers describing baryons, e.g. the strangeness $S = -(n_s - n_{\bar{s}})$, where $n_s, n_{\bar{s}}$ are respectively the number of strange quarks and anti strange quark in the system.

Hyperons form a subdivision of the baryon family and are defined as baryons that have one or more strange quarks with no top, bottom or charm quarks involved. An example of this kind of particle is the Λ particle which consists out of one up quark, one down quark, and one strange quark.

Aside from quarks, mesons, and baryons, Quantum chromodynamics (QCD), the quantum field theory that describes the strong interaction, allows for states that consist of more than three quarks. Such states are referred to as *exotic hadrons*.

In 2003, the Belle experiment at the KEKB collider discovered a four-quark state referred to as X(3872), with as content $c\bar{c}u\bar{u}$ [15]. This experiment marks the first discovery of exotic hadrons. This experiment has been confirmed by many other experiments. Since this discovery, many other exotic hadrons have been found over the years, such as a pentaquark state with a quark content of $c\bar{c}u\bar{u}d$ discovered at the LHCb in 2015 [16]. All of these found multiquark states involve a heavy quark and anti-quark. While these exotic hadrons have been discovered, in most cases the exact configuration of these hadrons is still unknown. For instance, a tetraquark may be made out of two loosely bound mesons or can be in a tightly bound state. The same goes for the pentaquark which may as well be a tightly bound state or a loosely bound state of meson and baryon.

The existence of a stable bound state of 6 quarks *uuddss* with a mass low enough to be stable, or with a lifetime greater than the age of the Universe, has been first introduced by G. Farrar in [1]. The particle with this state has been given the name 'Sexaquark' (S). The hypothesis of a quark state with the content of *uuddss* had already been introduced by R. Jaffe in 1976 and is referred to as the H-dibaryon. The hypothesis of the H-dibaryon will be discussed in section 4.1, together with the negative experimental results for the particle. This will be followed by a discussion of the properties of the S particle in section 4.2, arguments for the S to be a possible dark matter candidate in section 4.3, and finally the possible experimental searches for the particle, proposed by G. Farrar, are discussed in section 4.4

4.1 H-dibaryon

The possibility of a stable H-dibaryon with a quark content of *udsuds* could be the result of the combination of two *uds* hyperons and was proposed by R. Jaffe [17]. This particle is a positive parity state, spin, and isospin singlet state with baryon number $B = 2$ and strangeness $S = -2$. Jaffe calculated, using the MIT bag model, that the state has a mass 81 *MeV* lighter than the $\Lambda\Lambda$ threshold (= 2231 MeV / c^2), i.e. a mass of 2150 MeV/c^2. This means that the H-

dibaryon is stable against the strong interaction and can only interact via the weak interaction. Since the proposal of the H-dibaryon, many experiments with several different methods have been performed on a wide range of the particle's mass and lifetime to search for it. However, despite all the experiments, there has not been found conclusive evidence of the existence of the H-dibaryon. In fact, evidence against its existence has been found [18, 19, 20, 21, 22].

Observation from experiments involving the decay products of hypernuclei, which are nuclei that have at least one hyperon in addition to the normal protons and neutrons, can be used as an evidence against the existence of the H-dibaryon. An example of a double-hypernucleus decay is found at the KEK collider [23]. This was observed in a target that was exposed to a K^- beam. This event is interpreted as a decay of $_{\Lambda\Lambda}^{6}$He that was emitted from a Ξ particle that is created in the target from the interaction with the beam. The Ξ particles can interact with the material when they come to rest and can create a Λ^0 pair. By measuring the mass, the interaction energy of $\Lambda - \Lambda$ and the binding energy of two Λ hyperons was determined from which a lower limit on the mass of the H-dibaryon was found of $m_H > 2223.7$ MeV/c^2 at a confidence level (CL) of 90%. This observation thus excluded the original computed mass of Jaffe.

Furthermore, other evidence against the H-dibaryon can be found in observations from Υ decay. H-dibaryons may be produced in the decay of these particles and then further decay themselves, such as a process of $\Upsilon \to H + X$, $H \to \Lambda p^-$ or $H \to \Lambda\Lambda$. Observations of this process were made with the Belle detector at the KEKB e^+e^- collider and resulted in no evidence for this decay process in a small mass region around the $\Lambda\Lambda$ threshold [24].

Despite there being no evidence for a fairly loose-bound state of six quarks *uuddss*, It is still possible that this six-quark state is a rather strongly bound state, in contrast with the H-dibaryon. This is the case for the Sexaquark.

4.2 Sexaquark properties

The sexaquark particle is a hypothesized deeply bound six-quark state that is a spin-0, flavour singlet, parity-even boson that is electrically neutral, i.e. $Q = 0$, has baryon number $B = 2$ and Strangeness $S = -2$, as it contains two strange quarks. The reason that this particle state is of particular interest is due to the wave function that allows for favorable stability. Its spatial wave function is totally symmetric and its color, flavour, and spin wave functions are totally antisymmetric. This wave function describing the S provides arguments for this six-quark state to be the most tightly bound state involving its quark content.

The stability of the S particle depends on the mass of the particle. However, a good analog for estimating the mass of S based on hadron masses does not exist. There is no obvious implication for the mass of the particle from chiral symmetry breaking, as the particle is a scalar. Furthermore, there are no a priori relations to the masses of other known baryons to that of the mass of S. An example of this is the combination $K^-\bar{K}^+\pi^+$ that has the same quark content as an S particle and has a mass of $1130 MeV/c^2$. However, because the mesons are so-called pseudo-Goldstone bosons and the S particle is not, there is no reason to think why the particles should have the same mass.

Lattice QCD computations should be able to give an exact calculation of the S mass. However, recent calculations are far from a realistic six-quark state. Calculations for the mass have been performed and range from 1130 MeV/c^2 in Ref [25] to 2240 MeV/c^2 in Ref [26].

Most particle physicists find the six-quark state implausible because of an unjustified intuition from a non-relativistic weakly bound constituent quark model, namely that a mass of ~ 300 MeV/c^2 should be added for each valence light quark. Strange quark mass is < 100 MeV/c^2 and

light quarks have masses < 5 MeV/c^2 thus hadrons with these particles are highly relativistic bound states, showing that the quark model is not justified for use.

The stability for the six-quark state of S particles differs depending on the mass ranges of the particle and are as follows [27]:

- $2 \times$ BE $+ m_p + m_n$ - $m_e \approx 1860$ MeV/$c^2 < m_S < 2 \times (m_p + m_e) \approx 1878$ MeV/c^2 : with m_S the mass of the sexaquark, m_p, m_e, m_n the masses of proton, electron, and neutron respectively and BE the binding energy of nucleons in the nucleus. If the mass is below the upper limit, it is stable against the decay into two protons and the lower limit prevents the formation of S particles in the nucleus.

- $2 \times (m_p + m_e) \approx 1878$ MeV/$c^2 < m_S < m_p + m_e + m_{\Lambda^0} \approx 2055$ MeV/c^2 : In this mass range, the S particle can decay through doubly weak interaction process and if $m_S < 1890$ MeV/c^2 its lifetime is greater than the age of the Universe.

- $m_p + m_e + m_{\Lambda^0} \approx 2055$ MeV/$c^2 < m_S < 2 \times m_{\Lambda^0} \approx 2232$ MeV/c^2: The S particle is not stable in this mass range as it can decay through a single weak interaction.

- $m_S > 2 \times m_{\Lambda^0}$: The sexaquark can decay into two Λ^0 through a strong interaction process and is thus not stable.

It is clear that the sexaquark and nuclei must lie in the mass range of 1860 - 1890 MeV/c^2 for them to have a lifetime greater than the age of the Universe.
Another property of the sexaquark is its small spatial extent compared to mesons and baryons. This is due to the fact that the S particle does not couple to pions. An estimate of the radius for the sexaquark can be found using the information of charge radius and Compton wavelength of nucleons and by using the fact that the Sexaquark does not couple with pions but that the S-nucleon interaction goes through the exchange of a f_0, which is a light meson. A nucleon has a Compton wavelength of $\lambda_n = 0.2$ fm and a radius of $r_n = 0.9$ fm. The following formula for the radius of the nucleon is used :

$$r_n \approx \lambda_n + \frac{1}{2}\lambda_\pi, \tag{4}$$

with λ_π the Compton wavelenght for the pions and thus finding that $\lambda_\pi = 1.4$ fm. The same formula can be used for the Sexaquark but now with the fact that it does not couple to pions but to f_0 particles :

$$r_S \approx \lambda_S + (0 \rightarrow \frac{1}{2})\lambda_{f_0} = 0.1 \rightarrow 0.3 fm, \tag{5}$$

where $\lambda_{f_0} = 0.4$ fm and $\lambda_S = 0.1$ fm were used. The smaller size of the S compared to other hadrons also affects the interactions cross-section of the particle.

4.3   Sexaquark as a dark matter candidate

In Ref [1], G. Farrar pointed out that a stable S could be a potential good dark matter candidate. For this, the particle would essentially need all the requirements and should be able to give a solution to all the problems that dark matter should be able to resolve.
An important requirement to be a dark matter candidate is that it should be able to explain the relic abundance of dark matter, which is a measure of the remaining amount of particles that remain from the Big Bang. The number density of any particle was at a certain point in

the Early Universe in thermal equilibrium and can be found by solving the relevant Boltzmann equations that describe the statistical behavior of a thermodynamic system. On the timescale of the Universe, the production of S particles is supposed to happen at the QCD phase transition where the Universe goes from a quark-gluon plasma to consisting of hadrons. This happens when the temperature in the Universe goes from 170 MeV to 140 MeV. This drop in temperature happens due to the expansion of the Universe. Solving the Boltzmann equations at the end of this phase transition can give an estimate of the relic abundance of the S particle and the amount of S particles produced at this time is supposed to remain about the same today because the S particle cannot undergo break-up interactions, such as $\pi + S \to \Sigma + \Lambda^0$, due to its small size. Computations for the S relic abundance have been made in Ref [28] and [27]. In Ref [28], the ratio of dark matter relic abundance to the relic abundance of baryons $\Omega_{DM}/\Omega_{baryons} \sim 5.3$ can be naturally found in the case for the sexaquark model with a mass in the range of 1870-1880 MeV/c^2.

The sexaquark could also provide a natural solution for the core-cusp problem. Cosmological N-body simulations can perform computations to predict the density profile of galaxies. The core-cusp problem is the discrepancy between the density profile found in these simulations and the inferred density profiles of dark matter for galaxies. In most of the simulations, a density distribution is found with the density increasing towards the center [29, 30]. However, observations show that nearby galaxies have much shallower or even flat-density profiles [31, 32]. Dark matter candidates that self-interact can cause heat transfer from the dynamic parts of dark matter halos to the less dynamic parts and thus make the dark matter halo smoother. If the self-interaction cross section is in the range of $\sigma_{DM,DM}/M \approx 8 \times 10^{-25}$ - 1×10^{-23} cm^2 GeV^{-1} c^2, it could give a solution to the core-cusp problem.

It is a natural question to ask that if the sexaquark does exist, how it hasn't been detected yet. For certain properties of the interaction cross sections of the S particle, this can be explained. The S could thermalize in the atmosphere if it has the proper S-nucleon interaction cross-section. This could cause the energy deposit of the S to drop below thresholds for direct detection experiments.

Furthermore, balloon-based direct detection experiments could be inapplicable as the S particle could thermalize in interstellar gas.

In the non-interacting cold dark matter model, a problem arises known as the star formation quenching problem. Quenching is the process where a galaxy loses cold gas which in turn suppresses star formation. It is proposed in this model that the inclusion of supernovae and active galactic nuclei could serve as a source of heating transfer and thus as the mechanism for the quenching process. However, this does not explain the star formation rate coherently. Sexaquarks on the other hand could serve as a heat transfer mechanism by interacting with baryonic matter, causing extra heat in the baryonic matter.

Sexaquark dark matter could resolve other cosmological and astrophysical problems such as too-big-to-fail, baryon asymmetry, galactic curves discussed in section 2, etc. It should be noted that all these points remain hypothetical until this point and it is still debated if the S could resolve all or parts of the dark matter problems.

Even if the S particle fails to resolve the dark matter problems, the particle itself is an interesting state of matter and deserves further investigation.

4.4   S production channels

Possible discovery channels for the sexaquark have been pointed out by G. Farrar in [1] and they fall into two categories: a search channel based on the production of S particles in Υ decays,

similar to that for the H-dibaryon and search channels based on the interaction of $\bar{S}$ particles, which are created in hadron colliders, and material within the detector.

Firstly, experiments involving the Υ decay were already used for observations about the H-dibaryons, such as the Belle experiment. However, these methods are not applicable to the stable compound state of the sexaquark and thus a new approach is needed. The proposed discovery channel is as follows :

$$\Upsilon \to S\bar{\Lambda}\bar{\Lambda} \text{ or } \bar{S}\Lambda\Lambda + \text{pions and/or } \gamma. \tag{6}$$

The mass of the S particle can be reconstructed in this process by the 4-momentum conservation ($m_S^2 = m_\Upsilon - m_{\Lambda 1} - m_{\Lambda 1} - m_{\pi's\gamma's}$), as all the decay products except the S are reconstructable. The BABAR collaboration has performed a search for the sexaquark in the decay channel of Υ to $S\bar{\Lambda}\bar{\Lambda}$ in the mass range of $m_S < 2.05$ GeV/c^2 [33]. No significant signal was observed in the search and an upper limit has been placed on the branching fractions $\Upsilon(2S, 3S)$ of (1.2-1.4) $\times 10^{-7}$ at a confidence level of 90%.

Secondly, It is possible that Sexaquarks are produced in hadron colliders. However, the creation rate of S and $\bar{S}$ particles in these collisions is negligibly small, which has been estimated to be around $10^{-4} - 10^{-6}$ relative to the production rates of pions. Additionally, the Sexaquarks are expected to have a very low interaction probability. Thus a large dataset would be needed for the search of it. For this reason, the LHS is of particular interest because of its high luminosity. The $\bar{S}$ particles can annihilate with materials in the detectors or in the beampipe of the LHS, so the proposed search channels for the $\bar{S}$ particles created in proton-proton collisions are :

$$\bar{S} + p \to \bar{\Lambda}^0(\bar{u}\bar{d}\bar{s}) + \text{K}^+(u\bar{s})$$
$$\bar{\Lambda}^0 \to \bar{p}(\bar{u}\bar{u}\bar{d}) + \pi^+(u\bar{d}) \tag{7}$$

$$\bar{S} + n \to \bar{\Xi}_0^+ + \pi^-(\bar{u}d)$$
$$\bar{\Xi}_0^+ \to \bar{\Lambda}_0(\bar{u}\bar{d}\bar{s}) + \pi^+(u\bar{d}) \tag{8}$$
$$\bar{\Lambda}^0(\bar{u}\bar{d}\bar{s}) \to \bar{p} \ (\bar{u}\bar{u}\bar{d}) + \pi^+(u\bar{d})$$

$$\bar{S} + n(udd) \to \bar{\Lambda}(\bar{u}\bar{d}\bar{s}) + \text{K}_S^0(\frac{d\bar{s} - \bar{d}s}{2})$$
$$\bar{\Lambda}(\bar{u}\bar{d}\bar{s}) \to \bar{p} \ (\bar{u}\bar{u}\bar{d}) + \pi^+(u\bar{d}) \tag{9}$$
$$\text{K}_S^0(\frac{d\bar{s} - \bar{d}s}{2}) \to \pi^+(u\bar{d}) + \pi^-(\bar{u}d)$$

The decay products in all of these channels are reconstructable. So the interaction vertex of the $\bar{S}$ with the proton/neutron and the mass of the $\bar{S}$- nucleon system can be established using the information of the reconstructed particles.

4.5   Search for the sexaquark

In Ref [2], a first search for the sexaquark at the LHC has been discussed by J. De Clerq. For the discussed search, the production channel given in Eq. 9 was considered. The anti-Sexaquarks in the search channels are created in the proton-proton collisions in the LHC, where they can then

interact with the material within the CMS detector and the CMS detector itself can be used to measure the decay products.

A full analysis of the reconstruction efficiency and background rejection was done with the use of a signal simulation, as well as actual datasets from CMS were used to compute an upper limit on the the $\bar{S}$ production cross-section ($\sigma(pp \rightarrow \bar{S})$) times the cross-section for the $\bar{S}$ annihilation with a neutron that results in a K_S^0 and a $\bar{\Lambda}^0$ ($\sigma(\bar{S} + n \rightarrow K_S^0 + \bar{\Lambda}^0)$). This upper limit is given by the following equation:

$$[\sigma(pp \rightarrow \bar{S}) \times \sigma(\bar{S} + n \rightarrow K_S^0 + \bar{\Lambda}^0)] = \frac{N^{UL}}{\frac{N_{ev} \times <PU> \times (1-C)}{\sigma_{pp}} \times \epsilon_{reco} \times \epsilon_{fid} \times \epsilon_{BckCuts} \times N_n}, \quad (10)$$

where N^{UL} is the upper limit on the number of events after all selection cuts, $< PU >$ is the average pileup in the datasets used in the study, C is the overlap rate between datasets (as in this specific analysis, datasets were used that could contain the same events), ϵ_{reco} is the $\bar{S}$ reconstruction efficiency, N_n is the neutron column density of the materials in the detector, $\epsilon_{BckCuts}$ is the efficiency with which the $\bar{S}$ survives the background cuts and ϵ_{fid} is the efficiency for the signal to be contained in the fiducial region in which the systematic uncertainties are controlled.

In the performed analysis done by De Clercq, only interactions of $\bar{S}$ with the beampipe in the CMS were considered. However, further ideas to improve the sensitivity of the search have been discussed as well, such as including the interactions of the $\bar{S}$ particles with other material in the detector than the beampipe, e.g. the pixel detectors. The study in this thesis focuses on the reconstruction efficiencies of the $\bar{S}$ when pixel detectors are added and thus no datasets will be used.

The $\bar{\Lambda}^0$ and K_S^0 particles can decay in the CMS detector itself as their $c\tau$ is $\approx$ 7.9 cm and $\approx$ 2.7 cm, respectively [34]. These charged particles are referred to as V^0 particles and can be reconstructed with the use of the CMS tracker and the standard CMS reconstruction. However, the fitting for these particles had to be adapted so that the kinematics fit the signal of Eq 9. In this thesis, an analysis of the reconstruction efficiency and the kinematic properties of the particles involved will be performed using the same search channel for the sexaquark as in Ref [2], i.e. Eq 9. The goal of this work will be to make this analysis where in the first case, interactions with $\bar{S}$ and neutrons in only the beampipe are taken into consideration, and in the second case the possibility for the $\bar{S}$ to interact in further with detector material of the CMS detector will be considered. A comparison can be made of both cases to see the effect of the addition of the detector material in the simulation.

The expected impact of the addition of pixel material in the signal simulation has already been discussed in an approximate way in Ref [2]. By including the pixel layers, the nuclear interaction lengths increase with an order of $\mathcal{O}(10)$, meaning that more $\bar{S}$ interactions will be included. However, there will be lower reconstruction efficiencies for $\bar{S}$ that interacted in the pixel layers as the particle will have a large displacement, meaning that the daughter particles will have on average less hits in the detector and thus that there will be a loss in seeding and track reconstruction.

5   Signal simulation

In this section, the performed analysis of the signal simulation will be discussed as well as the results.

Firstly, the software algorithms involved in the signal simulation will be discussed in section 5.1. This part is split into two, the EPOS-LHC software used for the production generator for the $\bar{S}$ and GEANT4 that implements the interaction of $\bar{S}$ with matter.

In section 5.2, we will talk about the concept and requirements for generated particle signals to be reconstructable, the weighting factors applied in the simulations, the kinematics for the $\bar{S}$ and its interactions parameters.

In section 5.3, the interaction and kinematic variables will be discussed for the daughter and granddaughter particles of the $\bar{S}$.

From this point, the signal simulation involving the additional pixel detectors will be referred to as *pixel signal* and the signal simulation with only the beampipe present as the *reference signal*.

5.1   Toolkits used for simulation

It is an enormous challenge to create software frameworks and applications for high-energy and nuclear physics experiments. Accurate, large-scale simulations of particle detectors and hadron collisions in particle detectors are of great interest. Widely used in these frameworks are Monte Carlo (MC) algorithms that rely on repeatedly applying random samplings to produce results. These methods are extremely useful in the case of problems of stochastic nature and for simulating systems that consist of a large amount of degrees of freedom.

5.1.1   EPOS-LHC

High-energy particle collisions are very complex processes that result in a wide variety of final state particles, consisting of hadrons, neutrinos, leptons, etc. The software algorithms contain models and theories of certain physics, including hard and soft interactions, parton distributions, total and partial cross sections, etc. Analytic solution attempts for the whole physics system are hopeless for multiple reasons, such as the fact that perturbation theory is not applicable for QCD at low energy scales and due to the absurd largeness of the system.

Monte Carlo models are used for these high-energy physics such as PYTHIA at the LHC. PYTHIA is a framework used for the high energy collisions of elementary particles such as e^-, e^+, p $\bar{p}$ in many combinations [35]. However, PYTHIA fails to reproduce accurate distributions where particles with low transverse momenta or strange particle productions are involved.

The Sexaquark is a particle that is expected to have low transverse momentum when they are created in the proton-proton collisions at the LHC. Because these particles are the main focus of this thesis, a special fine-tuned version of the EPOS-LHC software is used for the minimum bias event generator that implements the $\bar{S}$ and S production in the collisions. EPOS uses a model where quarks are produced from a thermal description and then quarks can stochastically be combined into hadrons. A More detailed comparison of PYTHIA and EPOS-LHC is given in [36].

5.1.2   GEANT4 software

GEANT4 is a platform used for the simulation of the physics processes of particles passing through material, again based on Monte Carlo methods. GEANT was originally created by CERN, has since then had multiple upgrades and is used in multiple kinds of projects around

the world. GEANT4 is mainly used in high-energy particle and nuclear physics [37, ?, 39]. The toolkit includes processes for implementing geometry, visualization, etc. A Large number of different materials and particles as well as hadronic and electromagnetic processes are included in the platform.

The GEANT4 software is used in this thesis for the modeling of the $\bar{S}$ interactions with the materials inside the CMS detector. The generated events from the EPOS are used as inputs for this software. Besides implementing the $\bar{S}$ interactions with material, GEANT4 also computes these physics processes in material for all the particles involved in the search channel.

5.2 $\bar{S}$ interactions and kinematics

Firstly, we will discuss the simulated interactions of the $\bar{S}$ with the materials in the CMS detectors. As mentioned in section 4.5, the main goal of this thesis is to make a comparison of the results found from, in the first case, the simulation when pixel layers are included in the signal simulation with the second case, where only the beampipe is taken into account for possible $\bar{S}$ interactions.

5.2.1 Additional detector material

In section 3.2.1, the material layout of the Phase-1 inner tracking system has been discussed. The inner tracking system consists of silicon pixel detectors and silicon strip detectors. In this research, the pixel detectors will be included as extra material in the simulation (compared to the work performed in Ref [2]). These consist of four cylindrical barrel layers and forward disks, which will be added to the simulation. The properties of these layers are given in Fig 7.

BPIX			
Layer	Radius [mm]	z position [mm]	Number of modules
L1	29	-270 to $+270$	96
L2	68	-270 to $+270$	224
L3	109	-270 to $+270$	352
L4	160	-270 to $+270$	512
FPIX			
Disk	Radius [mm]	z position [mm]	Number of modules
D1 inner ring	45–110	±338	88
D1 outer ring	96–161	±309	136
D2 inner ring	45–110	±413	88
D2 outer ring	96–161	±384	136
D3 inner ring	45–110	±508	88
D3 outer ring	96–161	±479	136

Figure 7: radius, z-position values, and amount of modules for the barrel layer pixel detectors (BPIX) and forward pixel detectors (FPIX). [40]

It would have been possible to include more of the detector material for the $\bar{S}$ interactions but the choice to only take into account the pixel layers was made to optimize the search sen-

sitivity. There would be a great loss in track reconstruction for the daughter particles and $\bar{S}$ particle itself if the $\bar{S}$ would interact with material laying further away from the beamspot. There is a great secondary vertex displacement in this case thus the reconstruction would be far more difficult.

The $\bar{S}$ particle was added to the GEANT4 framework so that the interaction process of the $\bar{S}$ with a neutron could be implemented in the GEANT4 software such that a simulation of this can be made. This is simulated as a hadronic interaction and a two-body decay of the $\bar{S}$-neutron system to a K_S^0 and $\bar{\Lambda}^0$ particle.

The interaction cross section of the $\bar{S}$ with the matter is very low. This low interaction cross section means that a uniform interaction probability should be present throughout all of the material. This can be simply implemented in GEANT4 this way, but that would result in a lot of the $\bar{S}$ particle escaping through the beampipe and pixel detectors, which would not be optimal in terms of simulation process time. For this reason, a so-called *looping mechanism* is used in the simulation of the interaction process. This looping mechanism works as follows: A $\bar{S}$ particle is created in an event using the EPOS, in which the parameters such as momentum and creation vertex are given to the particle. Then the transport of the $\bar{S}$ is simulated throughout the detector volume. If the particle doesn't interact in a defined volume of the detector, i.e. if the particle goes out of a chosen boundary, the $\bar{S}$ is 'killed' and an exact copy of the $\bar{S}$ is made at the same creation vertex. This copy will then again go through the same process until it interacts within the defined boundaries. In this search, the $\bar{S}$ is killed if it goes radially beyond 16.5 cm or if it goes beyond $|z| = 160$ cm. These values are chosen such that the pixel detectors are included and because the $\bar{S}$ are not reconstructable for higher values of $|z|$.

The CMS detector layers that are included in this search consist of a variety of different elements. In Fig 8, a histogram is displayed that shows how many times the $\bar{S}$ interacts with a certain element in the material volume chosen for the looping mechanism. This histogram was made for a total of $1.4\ 10^6$ $\bar{S}$ at the generator level. It can be seen from the figure that most of the interactions happen with beryllium (Z = 4), carbon (Z = 6), oxygen (Z = 8), aluminum (Z = 13) and silicon (Z = 14). The beampipe is made out of beryllium and has a simpler form compared to the layout of the pixel detectors. It is radially at a value of $r = 2.17$ cm, and has a thickness of 0.8 mm. It is clear that most of the interactions happen in the beampipe.
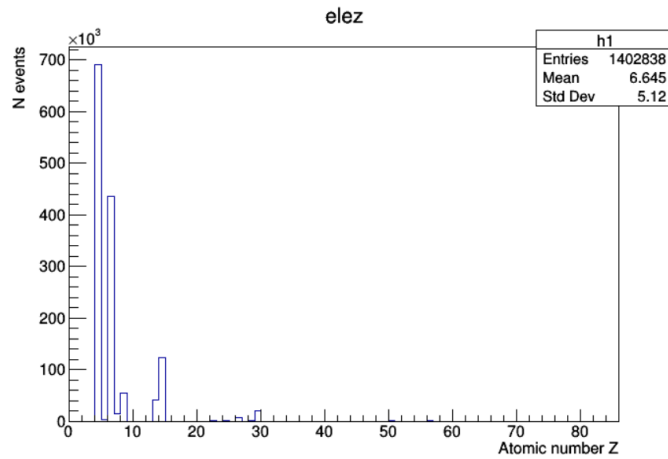
Figure 8: Histogram showing the number of times an element of the periodic table was encountered as interaction material for simulated $\bar{S}$ particles.

The looping mechanism makes sure that all the generated $\bar{S}$ interact somewhere in the included material. However, this is not realistic as the interaction probability will be larger for higher values of $|\eta|$, because the particles will then have larger paths through the beampipe. For this reason, an event-by-event weight factor is added, which is defined as $1/sin\theta_{\bar{S}}$. This weight factor will be referred to as the *eta weight*. Figure 9 shows the weight factor as a function of η of $\bar{S}$ and as a function of the z location of the interaction vertex of the $\bar{S}$.
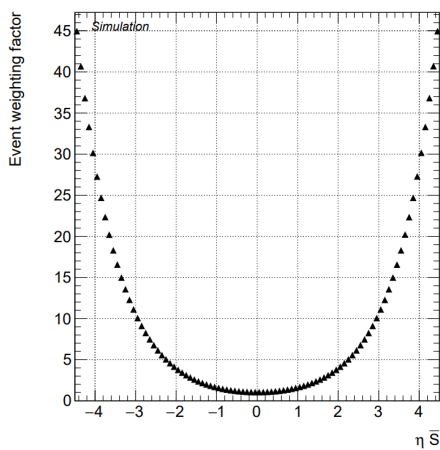
(a) η reweighting factor as a function of η of the simulated $\bar{S}$.
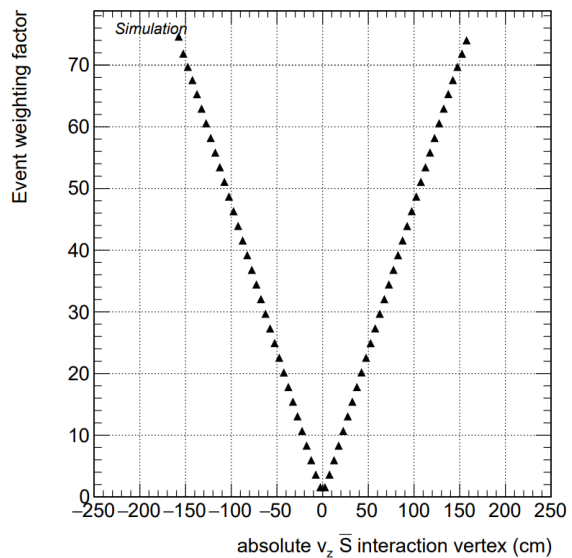
(b) η reweighting factor as a function of the longitudinal displacement of the interaction vertex of the $\bar{S}$.

Figure 9

5.2.2   Material reweighting

Another problem arises in the looping mechanism when additional material to the beampipe is included in the simulation. The $\bar{S}$ goes through this looping and killing process until it interacts somewhere in the defined volume. This will affect the original interaction distribution of the $\bar{S}$ in the beampipe. The extra material behind the beampipe will give a chance for the $\bar{S}$ to interact in that material, meaning that there are fewer interactions in the beampipe itself compared to the reference. This disruption of the interaction distribution is proportional to the amount of additional material that the $\bar{S}$ passes, given its parameters of momenta and creation vertex, up until it reaches the defined boundary values.

For this reason, a reweighting has to be done to account for this effect. This reweighting should thus happen in terms of the amount of material passed for each individual $\bar{S}$. This is done as follows: First, a large dataset of simulated $\bar{S}$ is used to create a *heatmap*, Fig 10 (a), of their interactions in the defined volume and to create a *density map* of the $\bar{S}$, Fig 10 (a). This density map is a heatmap that shows the density of the $\bar{S}$ paths from the dataset in the defined volume. To create this, first, an empty 2-D histogram is defined over the accepted volume in the detector. Then starting at the creation vertex of each $\bar{S}$ in the dataset, the position of the $\bar{S}$ is updated a tiny fraction using its momentum parameters given, and with every update, a value of 1 is added to the bin of the histogram corresponding to the position of the $\bar{S}$ at that update. By dividing the interaction heatmap with the density map, we are left with a 2D histogram that gives an approximation of the amount of material in each bin. The interaction heatmap, density map, and the division of both histograms are shown in Fig 10.

Using the division of the two histograms, which we will refer to as the material map, the reweighting factor for each $\bar{S}$ can easily be found. The procedure is as follows: For each individual $\bar{S}$, the position of the particle will be updated in tiny steps according to its direction of flight. Then for each step, the value of the bin corresponding to the position at the step will be added to either the variable *beampipe material* or *pixel material*, depending on whether the bin corresponds with beampipe material or pixel detector material, respectively. This keeps on going, step by step, until the $\bar{S}$ moves out of the previously defined volume. After all these steps, we are left with certain values for the variables *beampipe material* and *pixel material*. The final reweighting factor for each individual $\bar{S}$ is then given by

$$\text{Material reweighting } = \frac{\text{(beampipe material + pixel material)}}{\text{beampipe material}}. \tag{11}$$

In this way, the reweighting factor accounts for the amount of additional material passed by an $\bar{S}$ with respect to the amount of beampipe material passed and fixes the interaction distribution. Fig 11 the reweighting factor for the $\bar{S}$ is shown as a function of η. It can be seen on this figure that the reweighting factor works as expected. At the higher values of η, the value for the weight is 1 because at these values there is no other material found after the beampipe, as can be seen on the figure of the heatmap. Furthermore, it can also be seen that the particles with smaller $|\eta|$ pass through more additional material, also in correspondence with the heatmap.

From this Fig, it is clear that the reweighting factor for the $\bar{S}$ that travel more centrally is around the order $\mathcal{O}(10)$. This was expected as discussed in section 4.5.

(a) Interaction heatmap

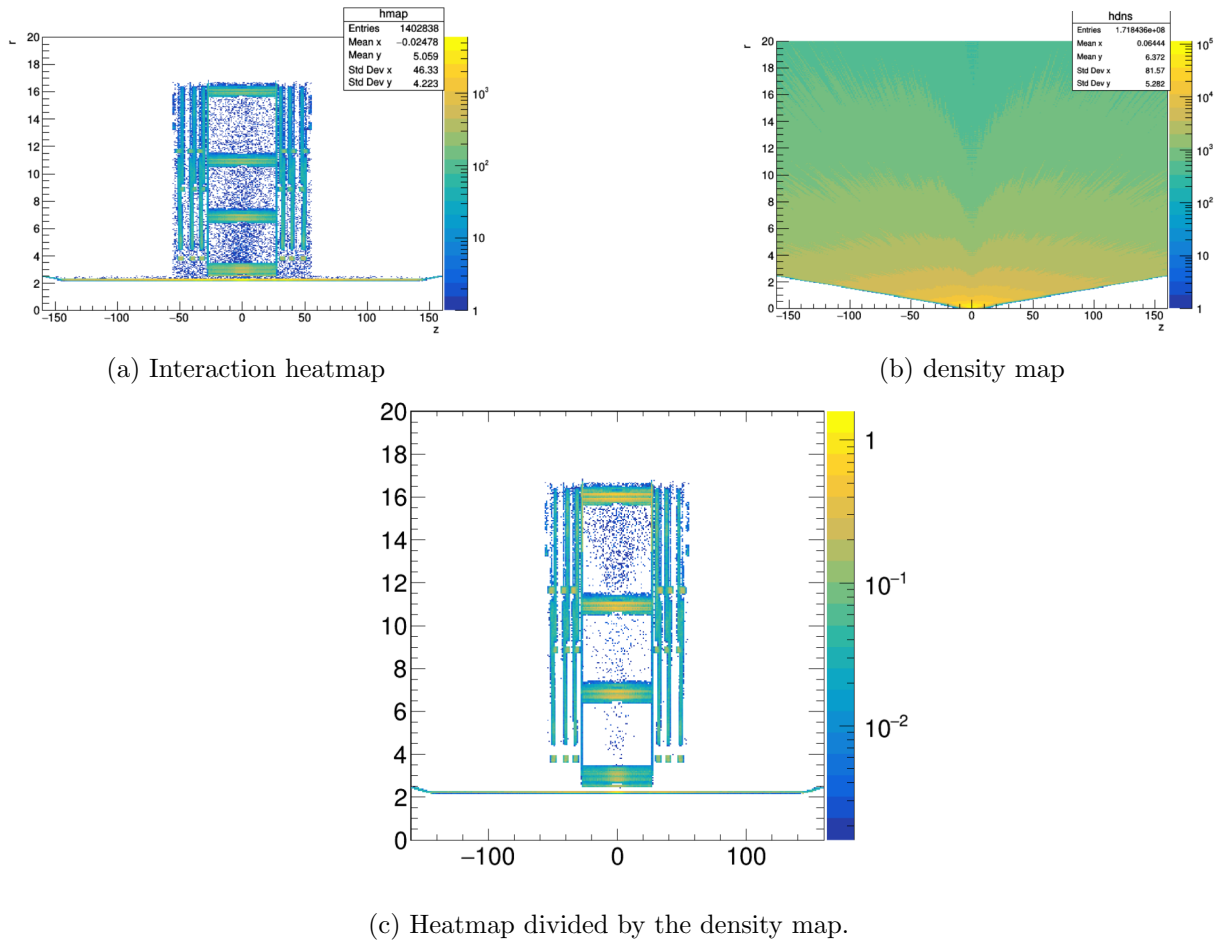(b) density map

(c) Heatmap divided by the density map.

Figure 10: Interaction heatmap (a), density map (b), and the division of both (c) of the $\bar{S}$
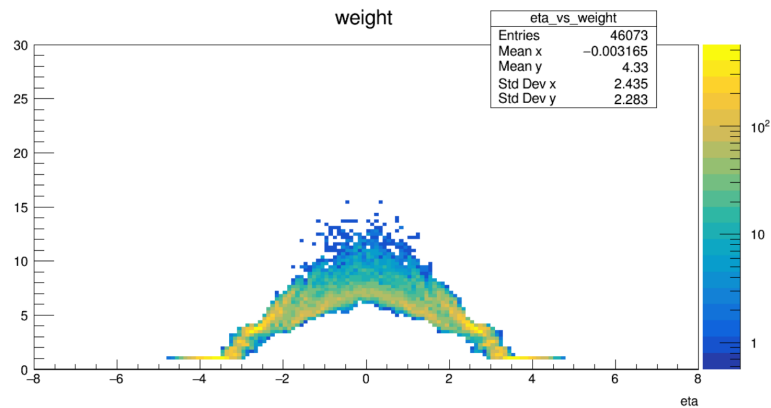

Figure 11: Distribution of the material reweighting factor in fucntion of the η of simulated $\bar{S}$.

Another weight parameter is applied to the signal simulation, which will be discussed in section 5.2.5 and is referred to as *primary vertex reweighting*. From this point on, all the results will have the eta weight and the primary vertex reweighting applied. This is true both in the case

for the reference signal simulation, i.e. the simulation where only the beampipe is included, and the pixel-included signal simulation. Additionally, the pixel-included signal simulation will from this point on also always have the material reweighting included, unless specifically mentioned.

5.2.3   interactions

Figure 12 shows the $\bar{S}$ interaction distributions found for the reference and pixel-included simulation in function of the x- and y-coordinates. The beampipe structure of the CMS is clearly present in both simulated interactions. It should be noted that in these simulations the beampipe center is put at the value of (x=0 and y=0), while in reality, it is a little bit off-center (x= 0.124 cm , y=0.027 cm) due to some complications in the installation of the beampipe. In the case of the pixel-simulated signal, the four barrel pixel detector layers are visible with details. From this representation, it can be seen that the barrel layers are not simple perfect cylindrical layers, but consist more of slightly overlaying parts connected together. The values of the radii for the pixel layers on this figure are in agreement with the values shown in the table of Fig 7. Furthermore, it can be seen that there are some outliers for the interactions, i.e. interactions that do not happen in the beampipe or the pixel layers. These interactions occur with gas molecules present in the detector. Interactions are not present within the beampipe itself because this part of the detector has been made vacuum with a high precision.
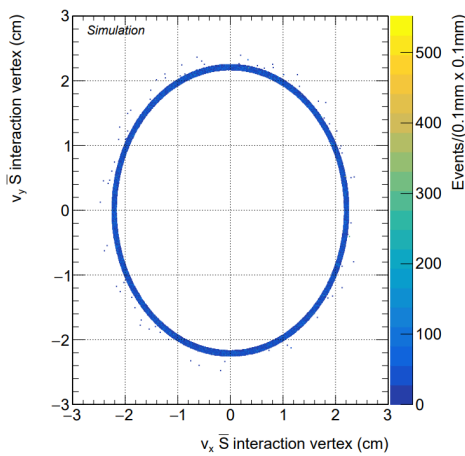
(a) Distribution of the interaction vertices of $\bar{S}$ in terms of x- and y- coordinates for the reference signal
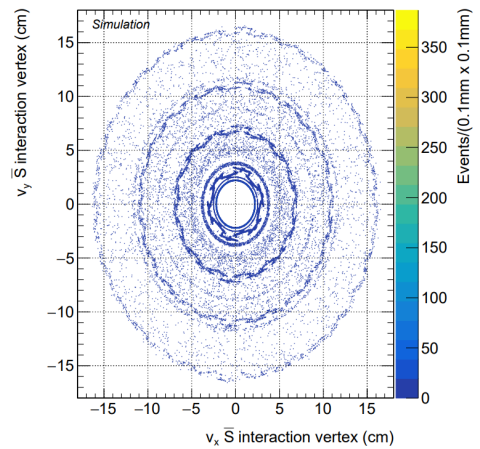
(b) Distribution of the interaction vertices of $\bar{S}$ in terms of x- and y- coordinates for the pixel-included signal.
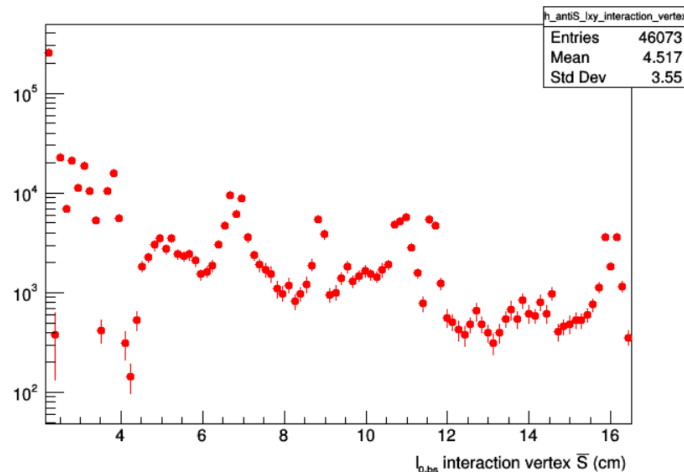
Figure 12

Figures in 13 show the interaction distributions for the $\bar{S}$ in function of the radius (defined as the variable l_0 on the graphs). In the reference simulated signal, a clear uniform probability can be seen throughout the entire beampipe, showing that the looping mechanism works properly. The pixel-included simulation does not directly show this uniform probability throughout the whole radius range, which is very much expected due to the fact that the density of the material is not uniform as well in this range. The beampipe is denser than all the other materials included and ranges from z = -160 cm to z = 160 in the simulation, meaning that there is way more

material included, and thus interactions, included in this radius region. The pixel detectors do not have this wide range in the z-direction (see Fig 7). Furthermore, the complex total structure of the pixel layers can be seen from the distribution. There are peaks in the distributions that correspond to the pixel layers. These peaks are found at the values of ≈ 7cm, ≈ 11cm , ≈ 16cm and thus correspond to the values of the pixel layers defined in Fig 7. Furthermore, a clear dip in the distributions can be seen at a value of ≈ 4 cm. When comparing this with the interaction heatmap created in Fig 10, this is expected as there is a very low amount of material present at that radius.
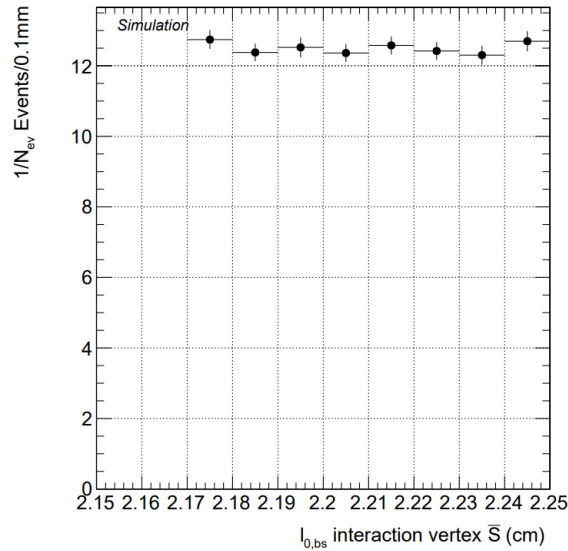
(a) Distribution of the interaction vertices of $\bar{S}$ in terms of x- and y- coordinates for the pixel-included signal.

(b) Distribution of the interaction vertices of $\bar{S}$ in terms of x- and y- coordinates for the reference signal

Figure 13: Interaction distributions of $\bar{S}$ in function of the radius $I_{0,bs}$ for the reference and pixel-included signal simulation.

Distributions for the number of loopings used before an interaction happened are shown in Fig 14, again for reference and pixel-included signal simulation. When the pixel layers are included, fewer loops are in general necessary to create a $\bar{S}$-neutron interaction. This is a normal effect to expect since more material will be encountered in a loop, meaning the chance is higher to interact per loop and thus fewer loops used to create an interaction.

The distribution for the number of loops when the $\bar{S}$ has an $|\eta| > 2.5$ have very similar values. This can be explained due to the fact that at these η values, $\bar{S}$ particles will not encounter any pixel detector material. Contrary, when interactions happen in the barrel region or endcap region, detector material will ofcourse be seen on its path.

(a)   (b)
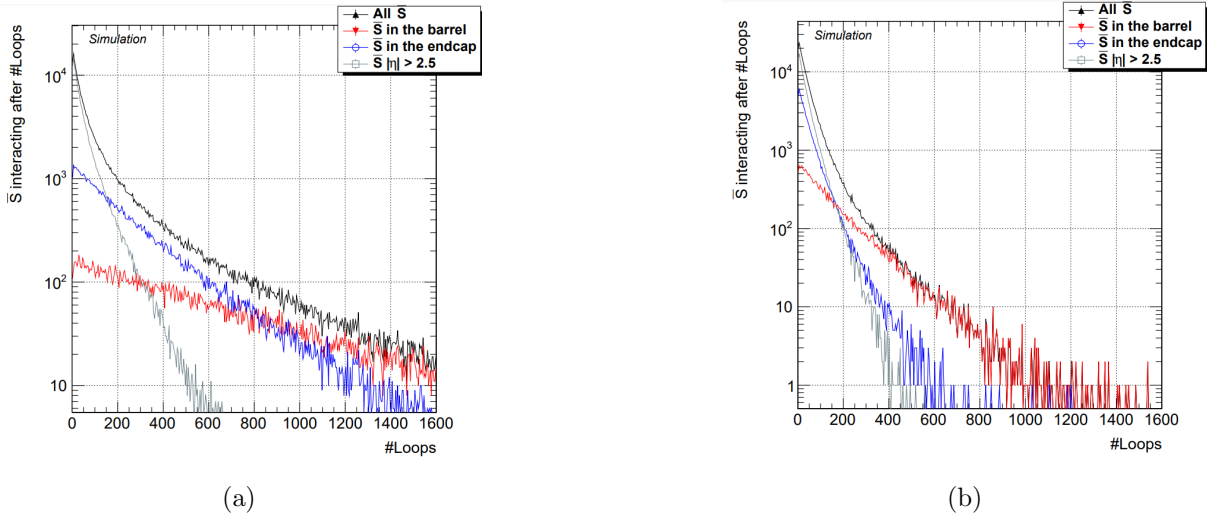
Figure 14: Distributions of the number of loops used until a $\bar{S}$-neutron interaction happened. a) reference signal simulation. b) Pixel-included signal simulation.

5.2.4 Fermi motion of the neutrons

An important fact that should be included in the simulation is that the neutrons in the materials are not stationary, but rather have a certain momentum distribution inside the nucleus. This is known as Fermi motion and is of order 200 MeV/c. This motion affects the accuracy of the reconstruction of the $\bar{S}$ properties, such as propagation direction and the invariant mass.

The Fermi motion distributions are different depending on the elements of the material. Despite this fact, the momentum distributions implemented in the signal simulation for the neutrons in the $\bar{S}$-neutron interaction is that of nucleons in a ^{9}Be nucleus [41]. Fig 15 shows the momenta distribution of the neutrons in ^{9}Be nuclei and in Oxygen nuclei. This is Beryllium Fermi motion is thus given to all the material included in the simulation. While this is the correct distribution for interactions happening in the beampipe, as this is made of beryllium, this might not be the case for interactions happening elsewhere. From Fig 8, it can be seen that many other elements are included in the material, such as carbon, oxygen, aluminum, and silicon. The ^{9}Be momentum distribution is used for all the materials because the information on the momentum distributions for the other materials was not yet available for implementation. The effects of using the momentum distributions corresponding to the correct elements of each type of material in the detector could be studied in further research. In Ref [41], these distributions are given for multiple elements and appear to have similar distributions.

Despite not having all the momentum distributions for the neutrons in all the different kinds of

materials present in the detector, a comparison is made between the reconstructed parameters in the presence of the momentum distribution of neutrons in ^{9}Be in the signal simulation, with the reconstructed parameters in the presence of the momentum distribution of the neutrons in Oxygen in the signal simulation. Using this, a check can be made to see if the deviations in these neutron momentum distributions cause large deviations in the reconstructed kinematics and efficiencies. When comparing the two distributions in Fig 15, it can be seen that the distributions are very similar. As will be shown in the next section, for certain kinematic parameters, the different fermi distributions will not have a visible effect on these kinematic parameters
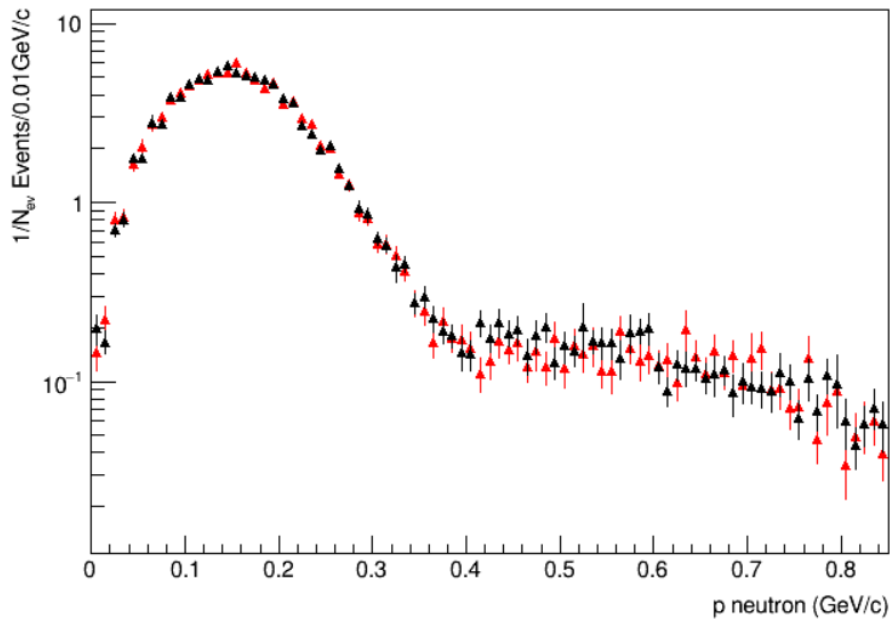
Figure 15: Momentum distribution of neutrons in Beryllium (black) and Oxygen (red).

In Fig 16 the correlation between the invariant mass $m_{\bar{S},obs}$ of the $\bar{S}$ and the magnitude of the vectorial sum of the momenta of K_S^0 and $\bar{\Lambda}^0$ is shown. This shows the influence of the fermi motion on the reconstruction of the invariant masses. In this plot, the assumption is made that the neutron is stationary for the calculation of $m_{\bar{S},obs}$. The calculations for the mass of the $\bar{S}$ are done here in the cases of reconstructable $\bar{S}$ events. A large spread of the invariant mass can be seen when the momenta of the K_S^0-$\bar{\Lambda}^0$ system increases. This spread can be so wide that even negative masses can be found. Negative invariant masses are here defined as occurrences where the vectorial sum of the final state particles squared is larger than the energy sum of the final state particles squared. The magnitude of the vectorial sum of the momenta of K_S^0 and $\bar{\Lambda}^0$ has been used for the correlation to the invariant masses here because this is the best proxy to the actual momenta of the $\bar{S}$ which can not be directly reconstructed. This thus shows that, due to fermi motion, the higher the momenta of the $\bar{S}$, the wider the spread will be on the invariant masses.
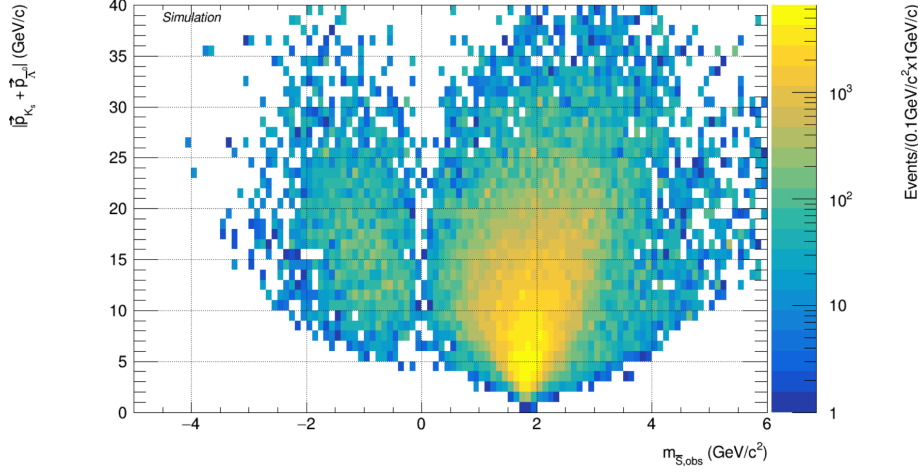
Figure 16: Plot showing the correlation between the invariant mass of the $\bar{S}$ and the magnitude of the vectorial sum of the momenta of K_S^0 and $\bar{\Lambda}^0$ for reconstructable events.

This result found from Fig 16 may feel counter-intuitive, but it can also be derived analytically. Suppose we have a neutron (n) at rest in the system with a mass m_n and an $\bar{S}$ with momentum $\vec{p}_{\bar{S}}$ and energy $E_{\bar{S}}$. The $\bar{S}$ annihilates with the neutron at rest, creating a K_S^0 and a $\bar{\Lambda}^0$ with energy and momentum E_{K_S}, $\vec{p}_{K_S}$ and $E_{\bar{\Lambda}}^0$, $\vec{p}_{\bar{\Lambda}^0}$ respectively. For this system, we calculate the following through energy-momentum conservation :

$$\left(E_{\bar{S}} \ , \ \vec{p}_{\bar{S}}\right) + \left(m_n, 0\right) = \left(E_{\bar{\Lambda}}^0 + E_{K_S} \ , \ \vec{p}_{\bar{\Lambda}^0} + \vec{p}_{K_S}\right)$$
$$\Leftrightarrow \left(E_{\bar{S}} \ , \ \vec{p}_{\bar{S}}\right) = \left(E_{\bar{\Lambda}}^0 + E_{K_S} \ , \ \vec{p}_{\bar{\Lambda}^0} + \vec{p}_{K_S}\right) - \left(m_n, 0\right), \tag{12}$$

After squaring both sides and performing a little further calculations, we now find

$$m_{\bar{S},obs} = \sqrt{(E_{\bar{\Lambda}^0} + E_{K_S})^2 + m_n^2 - 2m_n(E_{\bar{\Lambda}^0} + E_{K_S}) - (\vec{p}_{\bar{\Lambda}^0} + \vec{p}_{K_S})^2}, \tag{13}$$

where we used the energy-momentum relation $E_{\bar{S}}^2 = \vec{p}_{\bar{S}}^2 + m_{\bar{S},obs}^2$.
However, if we now include the fact that the neutron has a certain momentum, then we start off with the following equation :

$$\left(E_{\bar{S}} \ , \ \vec{p}_{\bar{S}}\right) + \left(m_n, \vec{p}_{\bar{S}}\right) = \left(E_{\bar{\Lambda}}^0 + E_{K_S} \ , \ \vec{p}_{\bar{\Lambda}^0} + \vec{p}_{K_S}\right)$$
$$\Leftrightarrow \left(E_{\bar{S}} \ , \ \vec{p}_{\bar{S}}\right) = \left(E_{\bar{\Lambda}}^0 + E_{K_S} \ , \ \vec{p}_{\bar{\Lambda}^0} + \vec{p}_{K_S}\right) - \left(m_n, \vec{p}_{\bar{S}}\right). \tag{14}$$

From this, we find that the invariant mass of the sexaquark in this case is given by :

$$m_{\bar{S}} = \sqrt{(E_{\bar{\Lambda}^0} + E_{K_S})^2 + m_n^2 - 2E_n(E_{\bar{\Lambda}^0} + E_{K_S}) - (\vec{p}_{\bar{\Lambda}^0} + \vec{p}_{K_S})^2 + 2\vec{p}_n(\vec{p}_{\bar{\Lambda}^0} + \vec{p}_{K_S})}. \tag{15}$$

If we now substitute the invariant mass found in 13 in the 14, we find the following :

$$m_{\bar{S},obs}^2 = m_{\bar{S}}^2 + 2(E_n - m_n)(E_{\bar{S}} + E_n) - 2\vec{p}_n(\vec{p}_{\bar{S}} + \vec{p}_n). \tag{16}$$

From this, it can clearly be seen that the mass difference ($m_{\bar{S},obs}^2 - m_{\bar{S}}^2$) is a function of the momenta of the sexaquark $\vec{p}_{\bar{S}}$ and thus that a higher momentum for the particle will lead to a wider spread on the reconstructed invariant mass.

5.2.5 $\bar{S}$ kinematics

The kinematics of the $\bar{S}$ without any reweighting factors are generated by the previously discussed EPOS-LHC software that includes the $\bar{S}$ in the proton-proton collisions. This is the first step in the signal simulation.

The pseudorapidity distributions for the $\bar{S}$ in the pixel signal and reference signal are shown in Fig 17. All the weight factors that are discussed in the previous section are included in these plots, i.e. material reweighting for the pixel signal, primary vertex reweighting and eta reweighting. This primary weighting factor is applied as the distribution of the z location of the valid primary vertices and the number of valid primary vertices per event is different in simulation and data [2]. A scale factor is applied to the pixel signal distributions such that the integral of the η distributions between $\eta = -8$ and $\eta = -4$ is the same for both signals because, as can be seen from Fig 11, at values $|\eta| > 4$ there is not material reweighting present anymore and thus the distributions should be the same at these values. When comparing the reference and pixel signal here, the influence of the material weighting factor is clear. In general, the transverse traveling $\bar{S}$ are more present when the material reweighting is included which is to be expected as there is much more pixel detector present central (in terms of η), and thus there will be a higher reweighting. Furthermore, two local bumps can be seen in the pixel signal at the location of $\eta = 2.5$ and $\eta = -2.5$. This can be explained by the distribution of the material reweighting factor in function of the η of the simulated $\bar{S}$, i.e. Fig 11. On this plot, it can be seen that there is a high density at the values of $\eta = 2.5$ and $\eta = -2.5$, meaning that there will be a lot of reweighting present at these locations, causing these local bumps. Lastly, it is clear that in both cases most of the $\bar{S}$ are produced forwards.

In Fig 18 the p_t and p_z distributions are shown for the simulated $\bar{S}$ in pixel and reference signal. From the p_t distributions we can see that the typical low values for the p_t for hadrons produced in the proton-proton collisions are also present in the kinematics of the $\bar{S}$ particles. This will lead to final state particles that will have low p_t values as well, thus giving a harder time in reconstruction. It can be seen on the p_t distribution that for the pixel signal, there are more $\bar{S}$ particles present with lower transverse momentum. This is to be expected because the material reweighting is bigger more centrally where the $\bar{S}$ with lower transverse momentum are more present centrally. For higher transverse momentum, the distributions follow the same low amount of events distributions.
For the comparison of the p_z distributions, it can be seen that the material reweighting does have an influence on its distributions, however, this effect is more random throughout the distribution where some parts of the pixel signal appear bigger or smaller than the reference signal.
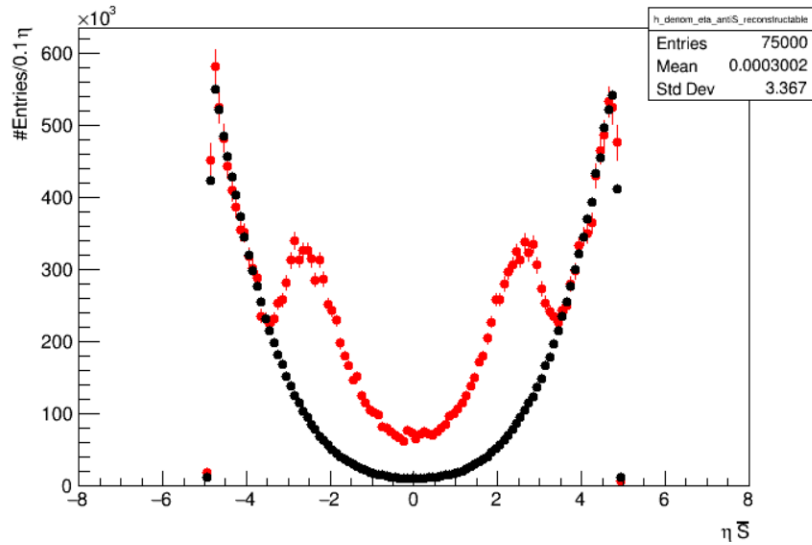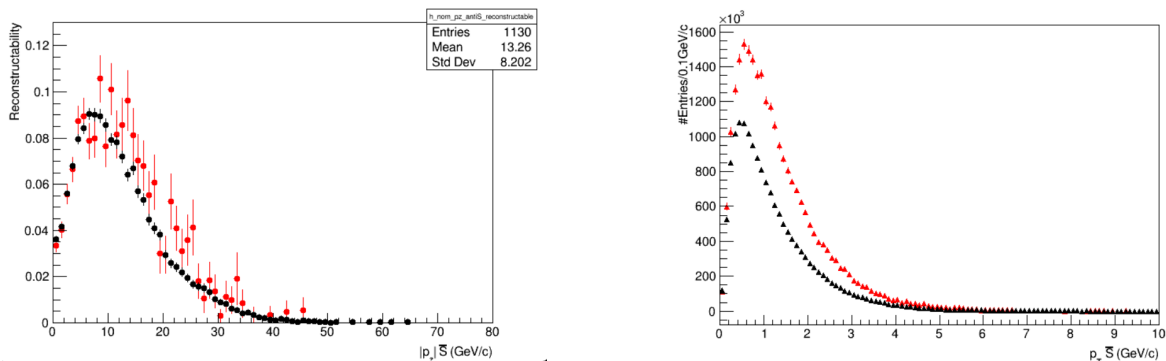
Figure 17: η distribution of $\bar{S}$ for the pixel signal (red) and reference signal (black).

(a) p_z distribution of the $\bar{S}$ for the pixel signal (red) and the reference signal (black).

(b) p_t distribution of the $\bar{S}$ for the pixel signal (red) and reference signal (black).

Figure 18: p_t and p_z distributions for the pixel and reference signals for all $\bar{S}$, i.e. reconstructable and non reconstructable $\bar{S}$.

5.2.6 Reconstructability

When trying to reconstruct a signal, efficiencies will be lost due to several factors which can be split up into efficiencies lost due to detector inefficiencies and efficiencies lost due to detector acceptance. There are three factors that have effects on signal reconstruction efficiency :

- Branching fraction: It is of course possible that the daughter particles do not decay into the desired granddaughter particles for the search. The branching fraction for $\bar{\Lambda}^0 \to \pi^+ \bar{p}$ is 63.9% and for $K_S^0 \to \pi^+ \pi^-$ is 69.2%, giving a combined percentage of 44.2%.

- Detector acceptance: The sexaquark interacts with the material to give a $\bar{\Lambda}^0$ and a K_S, which then further decays into anti protons and pions. These last four final state particles,

also referred to as granddaughter particles, should be in the tracker acceptance of the CMS tracker. This tracker acceptance is reached when each individual granddaughter particle has at least 7 hits in the tracker.

- Detector inefficiencies: Even if the previous two conditions are satisfied, there is no certainty that the $\bar{S}$ will be reconstructed. These inefficiencies will be further discussed in section 6.

$\bar{S}$ particles that satisfy the first two items discussed here are known as *reconstructable* Sexaquarks. Fig 19, 20, 21 shows the constructability of the sexaquarks as a function of the pseudorapidity, transverse and longitudinal momentum. This constructability is thus the probability of the $\bar{S}$ to be reconstructable. A comparison of the constructability for the pixel signal and reference signal is given in these figures. A clear difference in statistics is visible between the two. This is due to the fact that fewer events were used for the pixel signal. These plots include all the weighting parameters which will be discussed in the previous section.

When comparing the reconstructabilities for the pixel and reference signal, it can be seen that the reconstructability in the pixel signal is a little lower than that for the reference. This means that although it is lower, we can expect to see an increase in the number of reconstructable events when the many interactions in the pixel materials are added. For the p_t and p_z distributions, the differences are less clear to see. However, we can conclude that things look promising at the level of reconstructability.
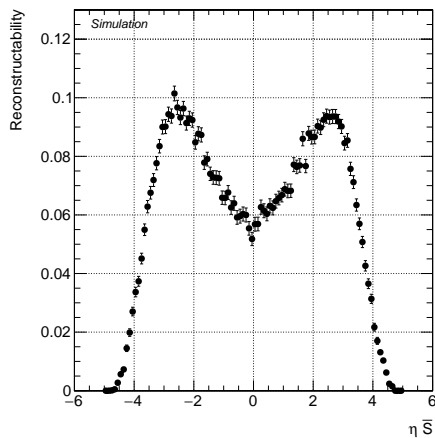
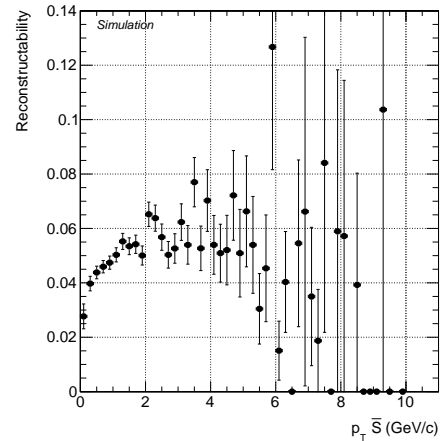(a) Reconstructability of the $\bar{S}$ in function of η for the reference signal
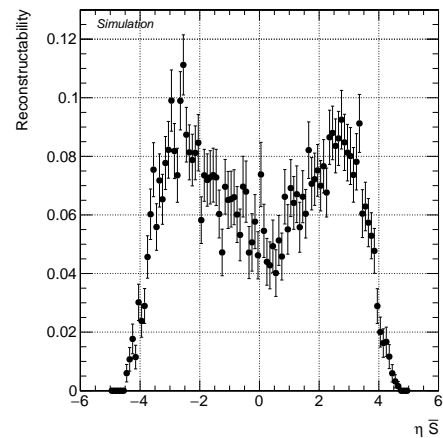
(b) Reconstructability of the $\bar{S}$ in function of η for the pixel signal
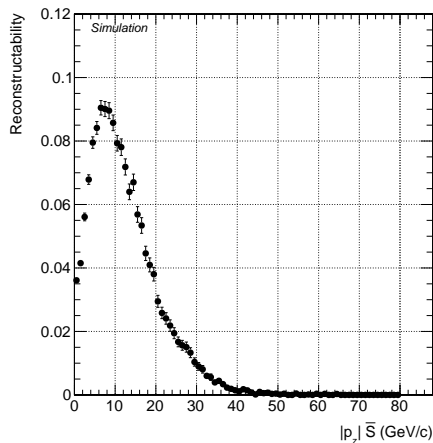
Figure 19: η reconstructabilities
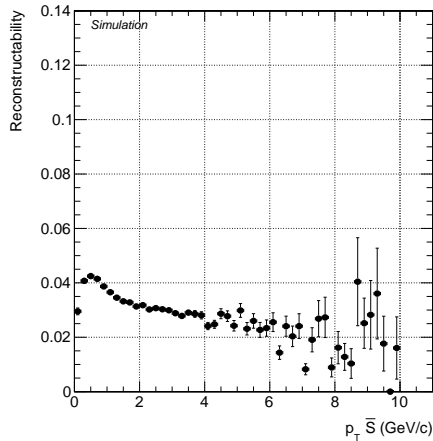
(a) Reconstructability of the $\bar{S}$ in function of p_t for the reference signal
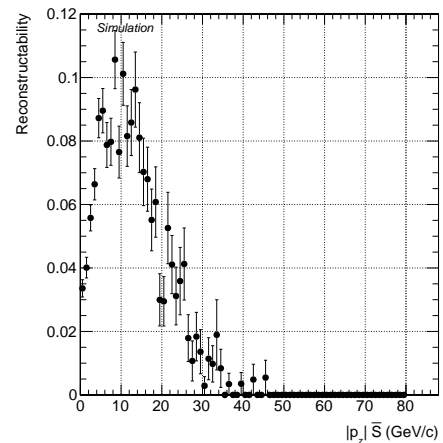

(b) Reconstructability of the $\bar{S}$ in function of p_t for the pixel signal

Figure 20: p_t reconstructabilities

(a) Reconstructability of the $\bar{S}$ in function of p_z for the pixel signal

(b) Reconstructability of the $\bar{S}$ in function of p_z for the reference signal

Figure 21: p_z reconstructabilities

5.3 V^0 interactions and kinematics

Just as studying the kinematics of the $\bar{S}$, a study of the daughter and granddaughter particles in the signal can also be informative and can be used to study the influence of adding the pixel detectors to the simulation. In this section, we will discuss the interactions and the kinematics of all the final state particles involved in the studied signal for the pixel and reference signal.

In Fig 22, 23 several plots of the creation vertices of the granddaughter particles are shown for the reference signal and pixel signal. These plots show a combination of the interaction vertex of the $\bar{S}$ particles and the decay lengths of the daughter particles $K_{\bar{S}}^0$ and $\bar{\Lambda}^0$.

From Fig 22, it can be seen that the transverse displacement of the creation vertices for the daughter particles of the $\bar{\Lambda}$ and $K^0_{\bar{S}}$ is in general higher for larger displacements for the pixel signal. When the pixel detectors are included in the simulation, the $\bar{S}$ particles can interact with material at higher transverse displacement, which thus causes more of the daughter particles to be able to travel further in transverse distance before decaying into the granddaughter particles. When comparing the graphs for the $\bar{\Lambda}$ with that for the $K^0_{\bar{S}}$, the creation vertices of the $\bar{\Lambda}$ have a distribution that is wider. This is to be expected by recalling that the decay length of the $\bar{\Lambda}$ is larger than that of $K^0_{\bar{S}}$.

The distributions of the longitudinal displacement of the creation vertices of the granddaughter particles are shown in Fig 23. Firstly, again the distribution for the daughter particles of the $\bar{\Lambda}$ has a wider spread compared to that of the $K^0_{\bar{S}}$. This is again due to the longer decay length of $\bar{\Lambda}$. Secondly, in all the distributions there are clearly two extrema visible. These extrema were also present in the longitudinal interaction displacement distribution for the $\bar{S}$ particles. This distribution is thus 'passed on' from the $\bar{S}$ to the creation vertices of the granddaughter particles. Finally, just as in the distribution for the longitudinal interaction displacements of the $\bar{S}$, the pixel signal distribution has a higher amount of events more centrally due to the material reweighting.
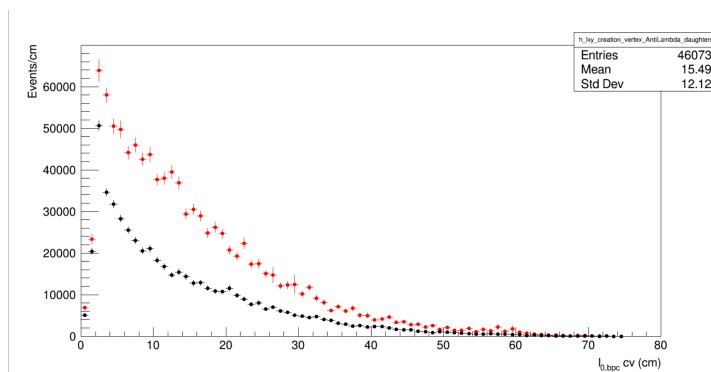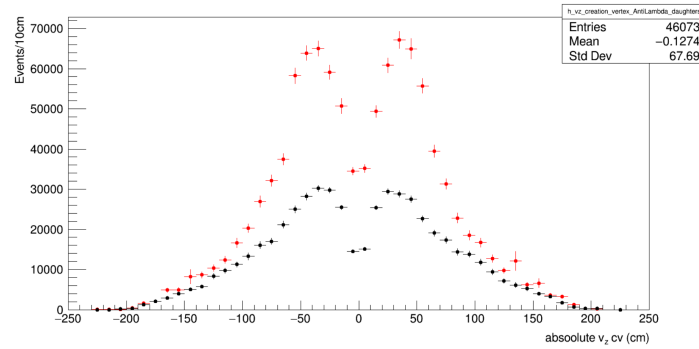

(a) Transverse displacement distribution for the $\bar{\Lambda}$ daughter particles for the reference (black) and pixel (red) signal.
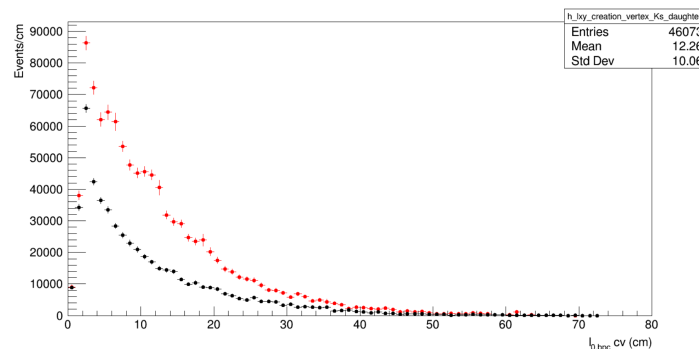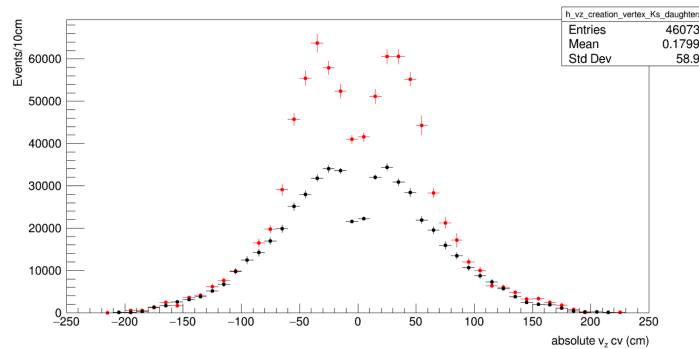

(b) Transverse displacement distribution for the $K^0_{\bar{S}}$ daughter particles for the reference (black) and pixel (red) signal.

Figure 22

(a) Longitudinal displacement distribution for the $\bar{\Lambda}$ daughter particles for the reference (black) and pixel (red) signal.
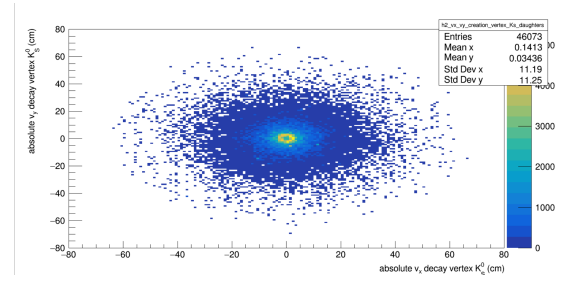

(b) Longitudinal displacement distribution for the $K^0_{\bar{S}}$ daughter particles for the reference (black) and pixel (red) signal.

Figure 23

Fig 24, 25, 26, 27 show the plots of the two-dimensional distributions of the creation vertices of the granddaughter particles. On the reference signal, there is a more concentrated amount of events closer to the beampipe, while for the pixel signal the distribution is more spread out. This is a healthy check that the pixel detectors are well included in the simulation. In Fig 27, 26, the forward movement of the daughter particles of the $\bar{S}$ is also visible. The longer decay length of the $\bar{\Lambda}$ can also be seen by comparing its distributions with that of the $K^0_{\bar{S}}$.
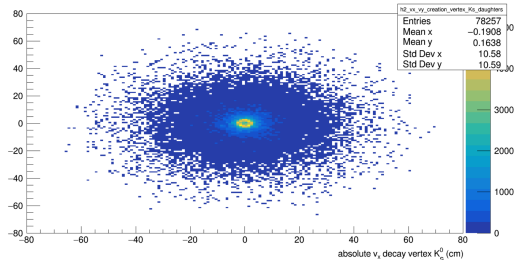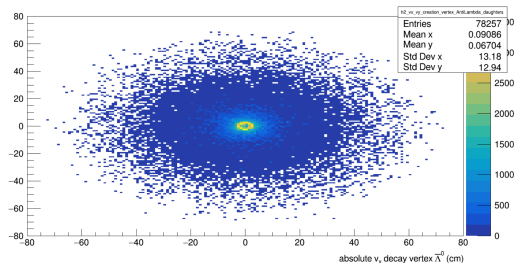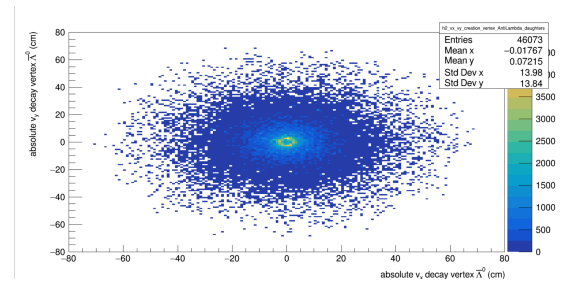
(a) Two dimensional distribution of the creation vertices of the daughter particles of the $K_{\bar{S}}^0$ in function of the displacement in the x- and y-direction for the reference signal.

(b) Two dimensional distribution of the creation vertices of the daughter particles of the $K_{\bar{S}}^0$ in function of the displacement in the x- and y-direction for the pixel signal.
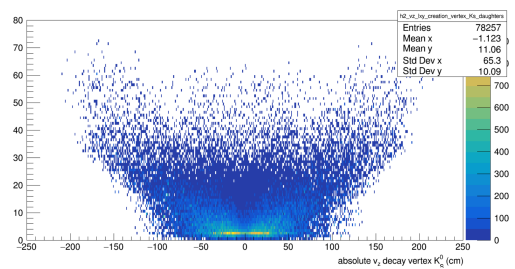
Figure 24

(a) Two dimensional distribution of the creation vertices of the daughter particles of the $\bar{\Lambda}^0$ in function of the displacement in the x- and y-direction for the reference signal.

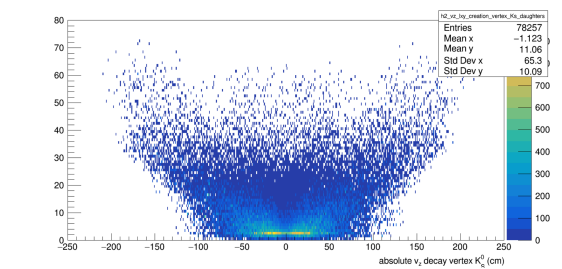(b) Two dimensional distribution of the creation vertices of the daughter particles of the $\bar{\Lambda}^0$ in function of the displacement in the x- and y-direction for the pixel signal.

Figure 25

(a) Two dimensional distribution of the creation vertices of the daughter particles of the $K_{\bar{S}}^0$ in function of the longitudinal and transverse displacement for the reference signal.
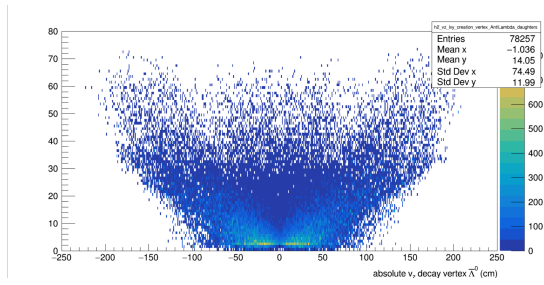

(b) Two dimensional distribution of the creation vertices of the daughter particles of the $K_{\bar{S}}^0$ in function of the longitudinal and transverse displacement for the pixel signal.
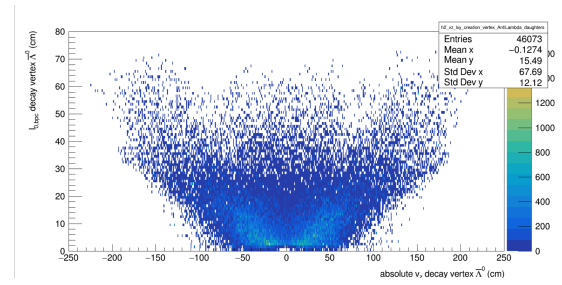
Figure 26

(a) Two dimensional distribution of the creation vertices of the daughter particles of the $\bar{\Lambda}^0$ in function of the longitudinal and transverse displacement for the reference signal.


(b) Two dimensional distribution of the creation vertices of the daughter particles of the $\bar{\Lambda}^0$ in function of the longitudinal and transverse displacement for the pixel signal.
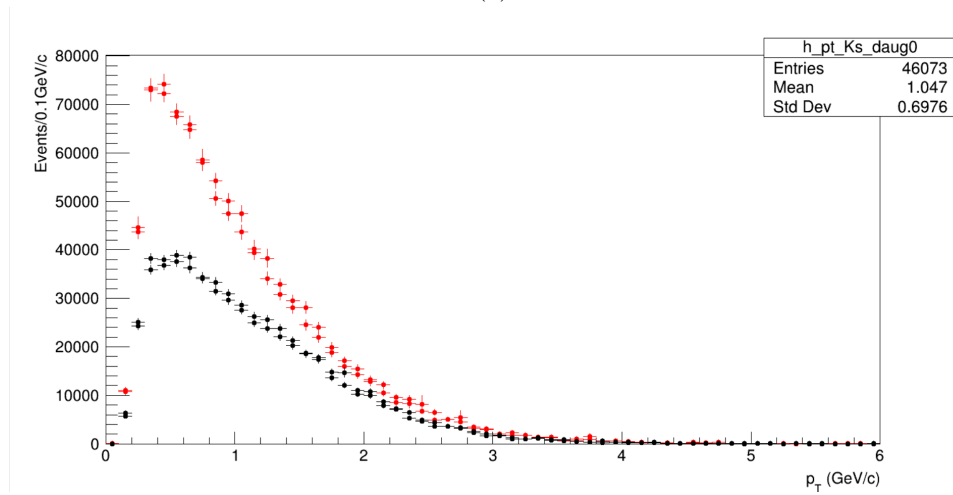
Figure 27

The transverse momentum distributions for the $\bar{\Lambda}$, $K^0_{\bar{S}}$ and their daughter particles are shown in Fig 28, 29, respectively, for the reference and pixel signals. All of these distributions show that the daughter and granddaughter particles of the $\bar{S}$ all have low p_t. It is important to note that the low p_t of these particles causes difficulty in the reconstruction of them as the CMS detector layout was designed for high p_t particles that could pass through many layers in the detector. Besides that, because the CMS was designed for high p_t particles, there is no trigger dedicated to the searched signal here. For this reason, in [2] all existing primary datasets were used together with the pileup interactions in the datasets for the signal search. This thesis focuses on signal simulation and reconstruction efficiencies, so no datasets will be used. While all the final state particles have low p_t it should be noted that this is especially true for the π^+, with its distribution ranging from $0 - 1.5$ GeV/c.

There are again changes in the distributions when pixel detectors and material reweighting are added. In general, the material reweighting causes higher peaks compared to the reference signal. The momentum distributions in the z-direction are shown in 30,31.
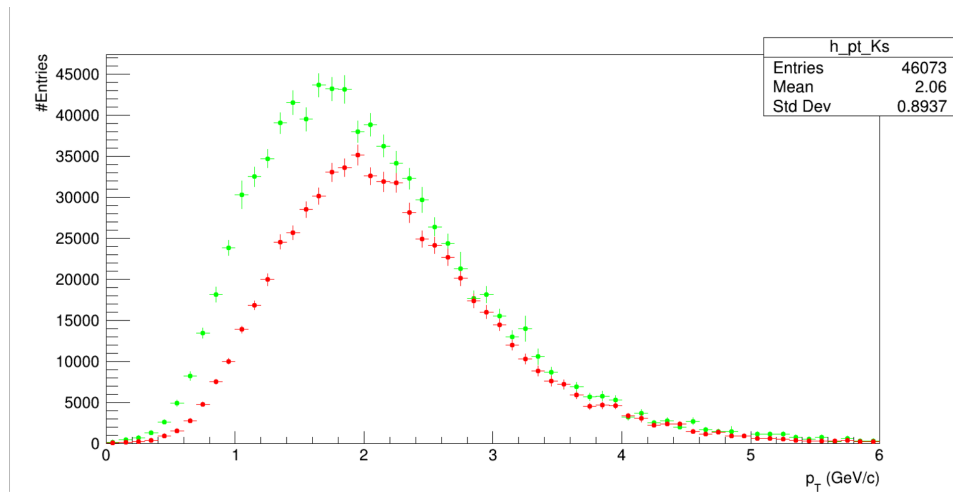
(a)

(b)

Figure 28: Transverse momentum distribution of the $K^0_{\bar{S}}$ (a) and the $K^0_{\bar{S}}$ daughter particles (b) for the reference and pixel signal. The pixel signal in (a) is given by the green distribution, while in (b) it is given by the red distribution.
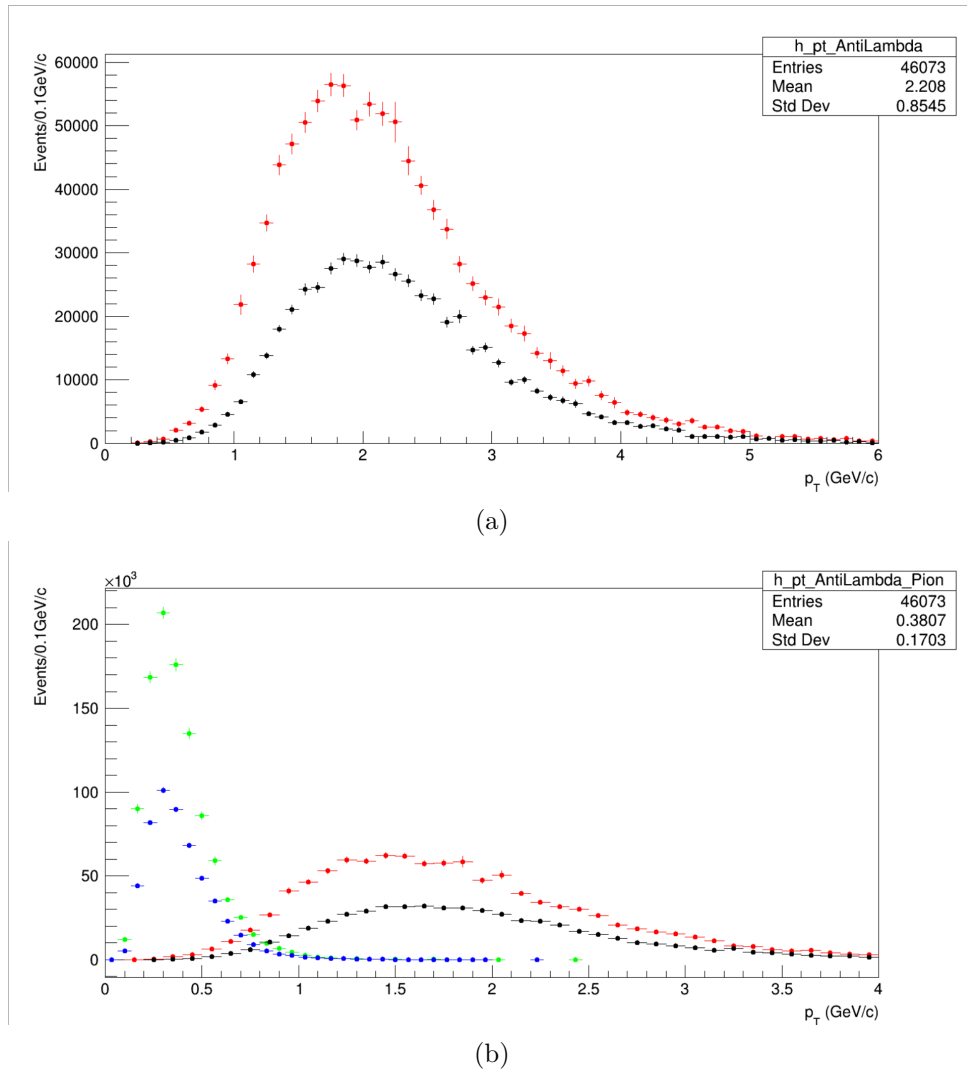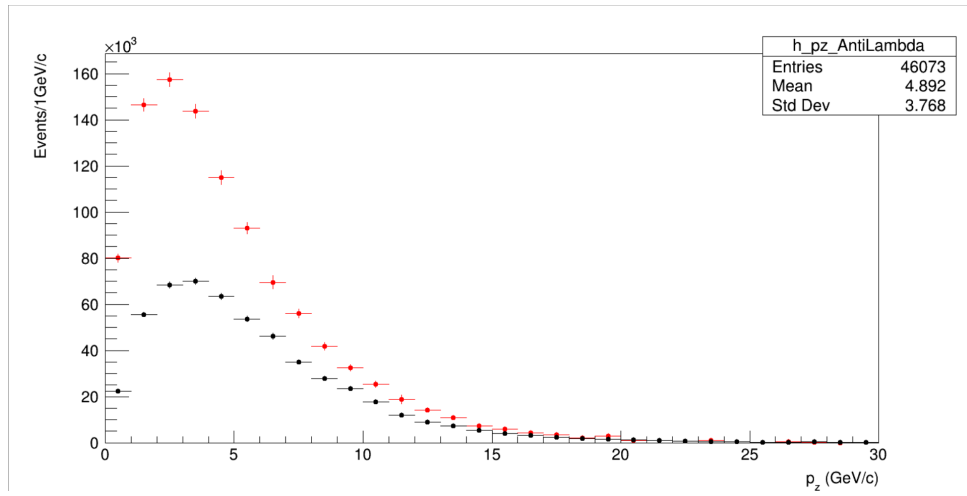
(a)

(b)

Figure 29: Transverse momentum distribution of the $\bar{\Lambda}^0$ (a) and the $\bar{\Lambda}^0$ daughter particles (b) for the reference and pixel signal. The pixel signal in (a) is shown in red. In (b) the pixel signal of the π^+ is shown in green and the reference in blue. The $\bar{p}$ is shown in red for the pixel signal and black for the reference.
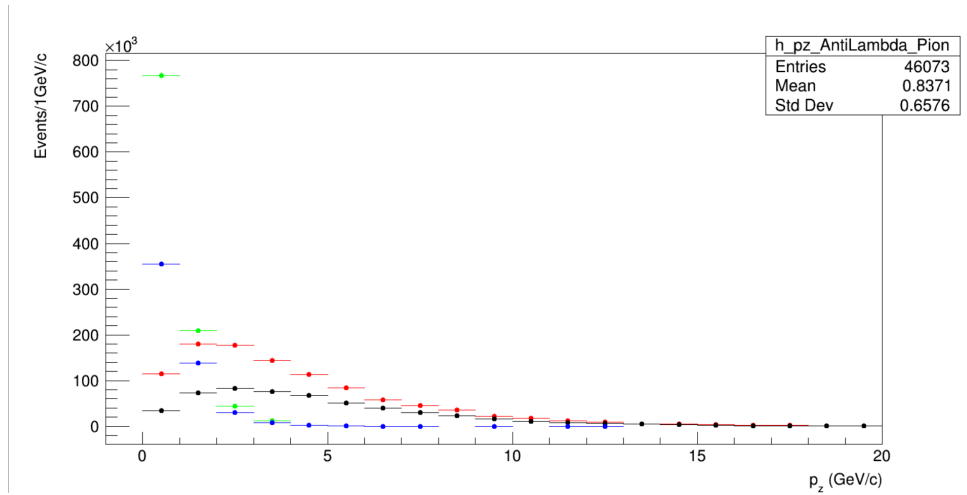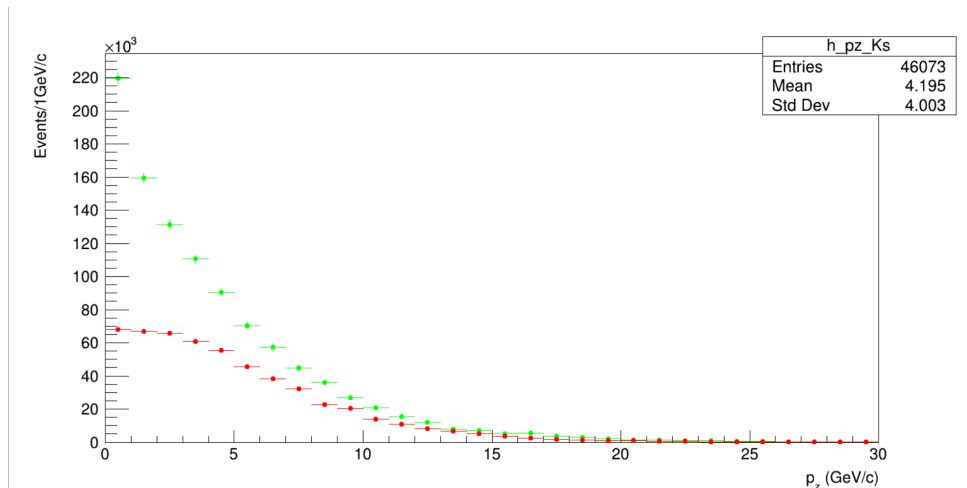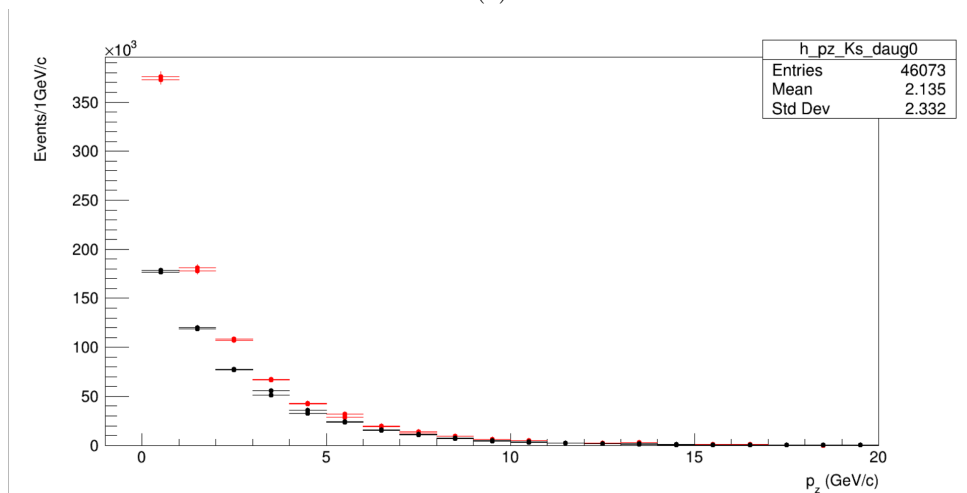
Figure 30: Momentum distribution in the z-direction of the $\bar{\Lambda}^0$ (a) and the $\bar{\Lambda}^0$ daughter particles (b) for the reference and pixel signal. The pixel signal in (a) is shown in red. In (b) the pixel signal of the π^+ is shown in green and the reference in blue. The $\bar{p}$ is shown in red for the pixel signal and black for the reference.

(a)

(b)

Figure 31: Momentum distribution in the z-direction of the $K_{\bar{S}^0}$ (a) and the $K_{\bar{S}}^0$ daughter particles (b) for the reference and pixel signal. The pixel signal in (a) is shown in green. In (b) the pixel signal of the daughter particles is given in red.

Fig 32 , 33, 34, 35 shows the transverse (d_0) and longitudinal (d_z) impact parameters of the $\bar{\Lambda}^0$, $K_{\bar{S}}^0$ and their daughter particles with respect to the beamspot. These are defined by the closest point of approach of a reconstructed trajectory of a track to the beamspot in the transverse and longitudinal plane, respectively. The sign of the transverse impact parameter is given by the scalar product of the vector connecting the beamspot and the creation vertex and the momentum vector.

Firstly, the distributions in all the plots show that the trajectories of the daughter and grand-daughter particles do not point undoubtedly toward the luminous region. This is of course the effect of the creation vertices of the $\bar{\Lambda}^0$ and K_S^0 being a secondary vertex in the search signal.

Secondly, when comparing the transverse impact parameter distribution of the reference, an interesting effect can be seen. In the reference signal, the transverse impact parameters of the $\bar{\Lambda}^0$ and $K_{\bar{S}}^0$ are bounded at about $|d_0| < 2.5\ cm$. When the pixel material is included, this bound is clearly not present anymore but now it ranges all the way from d_0 less than -10 cm to more than

+10 *cm*. This extra presence of the distribution between -10 *cm* and -3 *cm* can be explained as follows: In the reference signal, the $\bar{S}$ particles are obligated to interact in the beampipe in the simulation which lays at about 2.21 *cm* of the beam spot in the transverse distance. No matter what the trajectories of the daughter particles would be, the closest point to the beamspot would have to be maximally the interaction vertex of the $\bar{S}$. For the granddaughter particles, a larger transverse displacement is possible due to the fact that they are created further from the beamspot.

For the longitudinal impact parameter, this is not the case, as shown in Fig 34 , 35. Here we can see that the longitudinal impact parameters range from about -150 to 150 *cm*. It is possible that the daughter particles of the $\bar{S}$ closest point to the beamspot in the z-direction is far because the $\bar{S}$ can react as far as $|z| = 150$ in the beampipe which means that the longest longitudinal impact parameters can lay somewhere close underneath $|z| = 150$ *cm*. The influence of the pixel detectors can here also be seen in the range of $|z| = 60$, as the distribution can be seen to be a little more narrow with the tails of the distributions being lower when the pixels are added.

(a)   (b)

Figure 32: Transverse impact parameter of the creation vertices of $\bar{\Lambda}$ and its daughter particles. Reference signal left (a), pixel signal right (b).

(a) (b)

Figure 33: Transverse impact parameter of the creation vertices of $K_{\bar{S}}$ and its daughter particles. Reference signal left (a), pixel signal right (b).
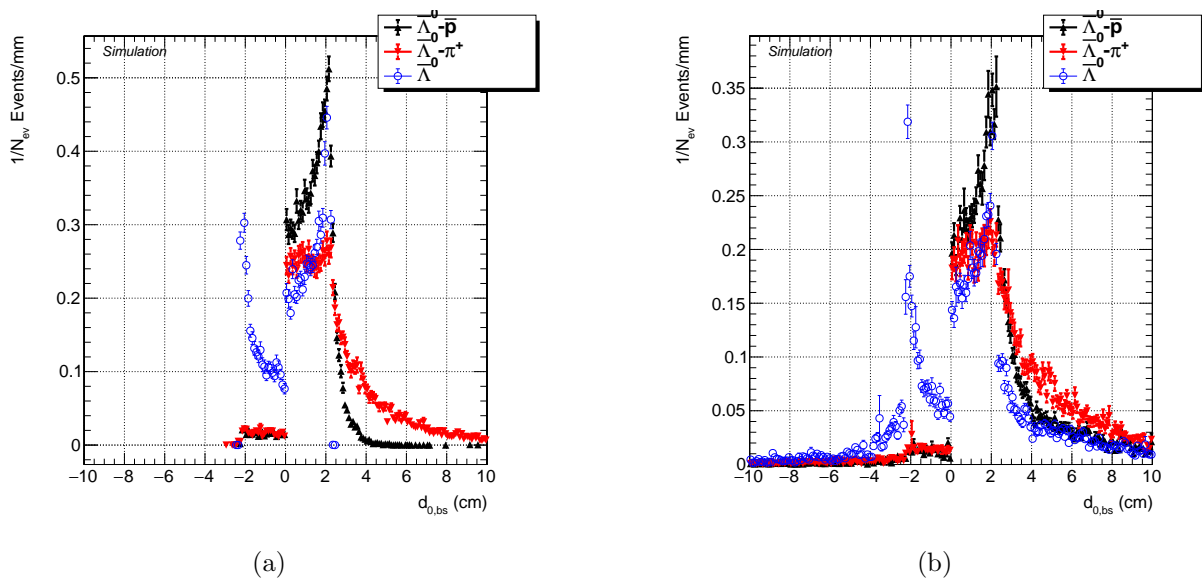

(a) (b)

Figure 34: Longitudinal impact parameter of the creation vertices of $\bar{\Lambda}$ and its daughter particles. Reference signal left (a), pixel signal right (b).

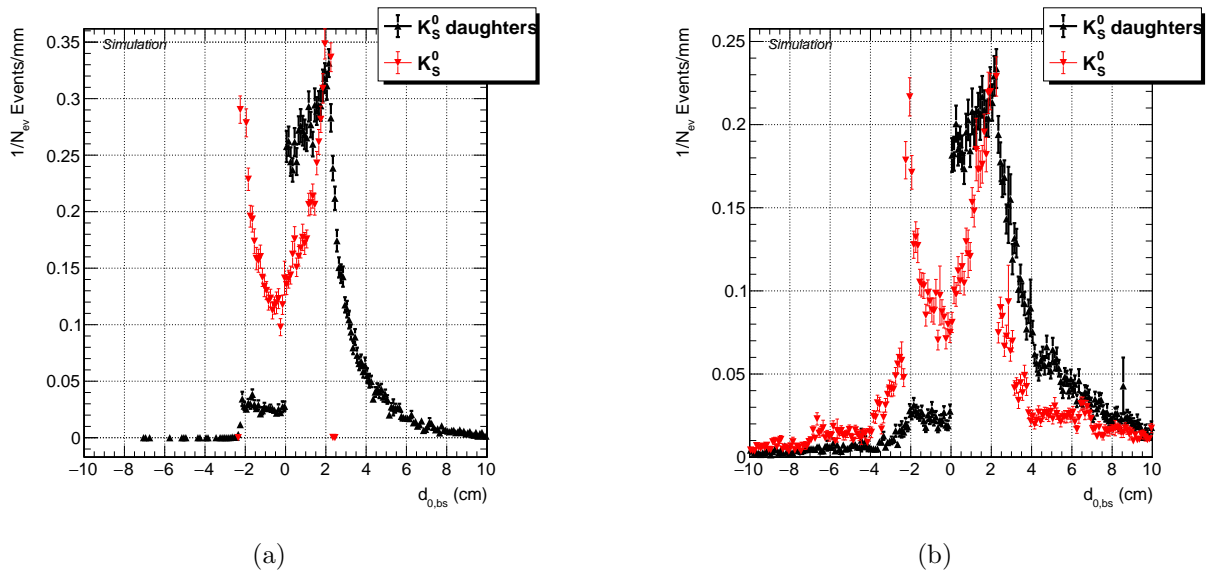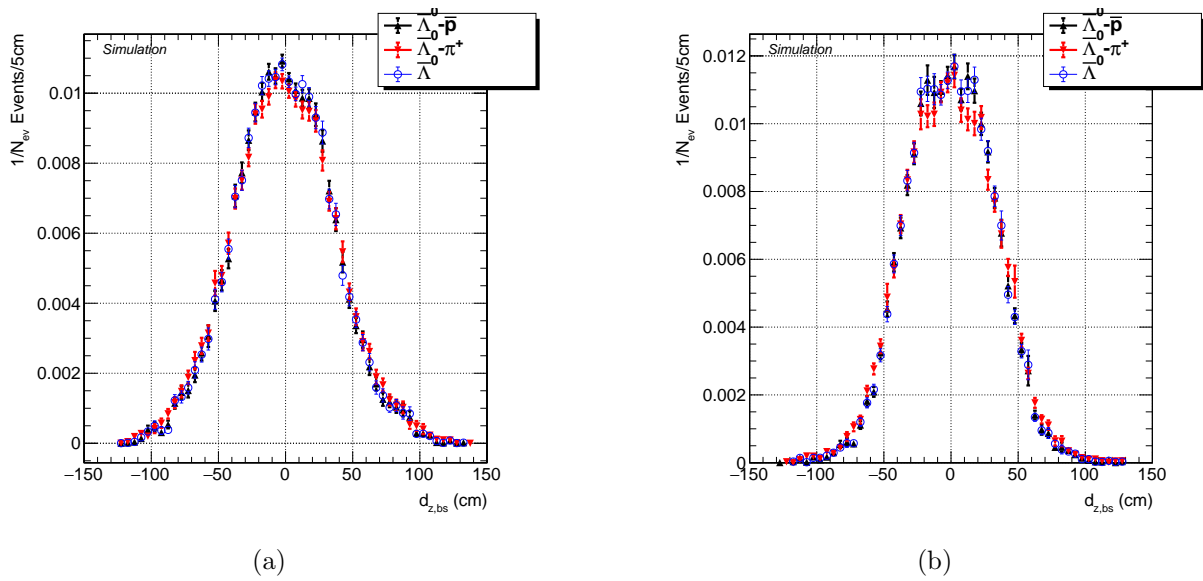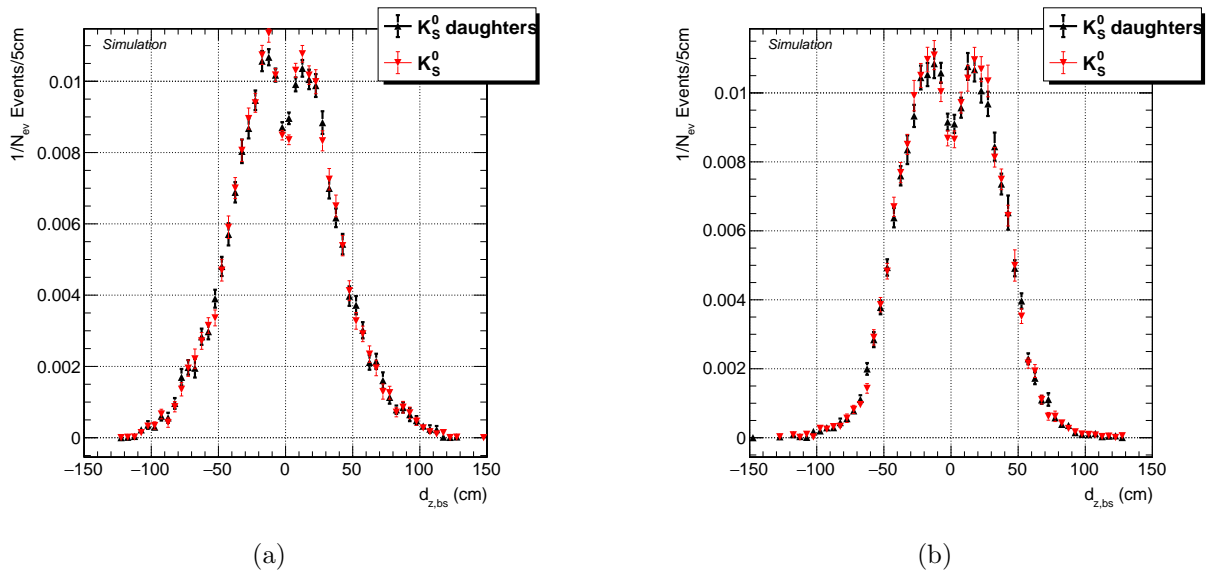Figure 35: Longitudinal impact parameter of the creation vertices of $K_{\bar{S}}$ and its daughter particles. Reference signal left (a), pixel signal right (b).

5.3.1   Fermi motion influence on kinematics

In the previous sections, Fermi motion for Beryllium was used for all the material in the signal simulation to create all the vertices and kinematic parameter distribution. However, as mentioned earlier in section 5.2.4, this should not be the case and all the different kinds of material should have their own fermi motion corresponding to the material it is built out of. Yet, when comparing the Fermi motion distributions of Beryllium and oxygen, they looked very similar. However, it can not be excluded that these small deviations from the distributions do not have an effect on the parameters in the simulation.

In this section, we will compare a few of the kinematic variables for the daughter and granddaughter particles when the Fermi motion for oxygen or for beryllium is applied.

Fig 36 shows the transverse momentum distributions of the $\bar{\Lambda}^0$ and the $K_{\bar{S}}^0$ in the case of oxygen and beryllium. The distributions on this plot both look very similar, implying that the different Fermi motion does not have any significant effect on these kinematic variables in the simulation. The transverse momenta were also checked for final state particles such as the $\bar{p}$ daughter particle of the $\bar{\Lambda}^0$ and for one of the daughter particles of the $K_{\bar{S}}^0$ and are shown in Fig 37. Also here there is no difference in the distributions visible.
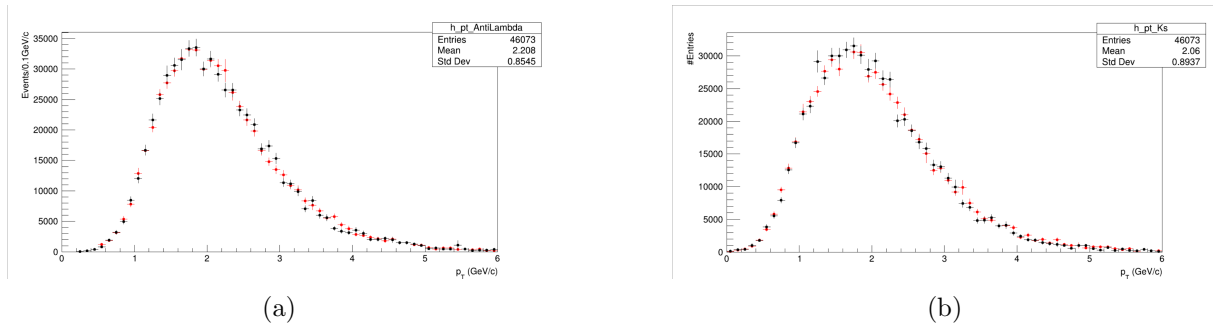
Figure 36: Transverse momentum distributions for the $\bar{\Lambda}$ (a) and the $K^0_{\bar{S}}$ (b) for a signal simulation with Fermi motion of beryllium included for all the material (black) or for oxygen (red)
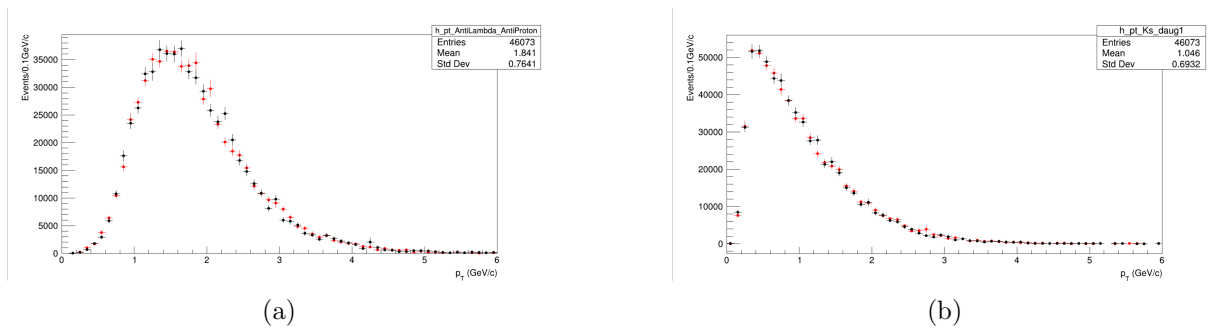
Figure 37: Transverse momentum distributions for the $\bar{p}$ (a) and of one of the daughter particles of the $K^0_{\bar{S}}$ (b) for a signal simulation with Fermi motion of beryllium included for all the material (black) or for oxygen (red).

While these kinematic variables show that the difference in Fermi motion for beryllium and oxygen does not have an influence on them, this is of course still not enough study to justify that the Fermi motion of beryllium could be used for all the material in the detector. In Fig 5.2.4, it can be seen that the distributions for the neutron momentum in the nuclei for oxygen and Beryllium are very similar. This however does not exclude that for different kinds of materials, these distributions might not look that similar. A further study is needed to investigate the different Fermi motion distributions for the different kinds of materials in the detector to be able to strongly say that using only the distribution for Beryllium is justified or if all the different Fermi motions are necessary.

6   Reconstruction efficiencies

In the previous section, the kinematics and interactions of the particles involved in the search signal were discussed for reconstructable $\bar{S}$ particles in the signal simulation. In this section, we will discuss the reconstruction efficiencies of the $\bar{S}$ in function of certain parameters. This will also be discussed for its daughter and granddaughter particles.

As mentioned in section 5.2.6, an $\bar{S}$ particle is called reconstructable if it passes through the first two bullet points given in the section. However, it is still possible that the particle is not reconstructed due to detector inefficiencies. It is these efficiencies that will be studied here. Matching simulated particles with reconstructed particles will be used to study the reconstruction efficiencies of all the particles. This is done by setting up certain matching conditions. These conditions are shown in Table 1. In this Table, $\Delta L_{xyz,dv}$ and $\Delta R(\vec{p}_{SIM,S}, \vec{p}_{RECO,S})$ are defined as the distance between the simulated and reconstructed decay vertex of the V^0 particles and the angular separation between simulated and reconstructed momentum direction of the V^0 particles, respectively. The subscript dv and iv refer to 'decay vertex' and 'interaction vertex'.

Particles	Matching condition
$\bar{S}$	All final state particles and all daughter particles matched,$\Delta R(\vec{p}_{SIM,S}, \vec{p}_{RECO,S}) < 0.5, \Delta L_{xyz,iv} < 2$cm
$\bar{\Lambda}^0$	$\Delta L_{xyz,dv} < 2$cm and $\Delta R(\vec{p}_{SIM}, \vec{p}_{RECO}) < 0.03$.
$K^0_{\bar{S}}$	$\Delta L_{xyz,dv} < 3$cm and $\Delta R(\vec{p}_{SIM}, \vec{p}_{RECO}) < 0.03$.
Final state particles	Above 75% of the reconstructed track hits should be matched with the simulated hits.

Table 1: Matching conditions for all the particles in the search signals [2].

With the use of these matching conditions, reconstruction efficiencies can be discussed in function of kinematic variables. We will discuss here a few of the results, once again for reference and pixel signal to compare. This study for the reference signal also has been done in [2], However, in this study, the number of events used in the signal simulation is significantly lower here, which causes a large decrease in statistics. As this thesis serves as a study of the effect of adding pixel detectors to the simulation compared to the reference signal study also made in [2], most of the same results will be discussed here with additional interesting effects. Firstly, the π^+ final state particle of the $\bar{\Lambda}^0$ has the lowest transverse momentum of all the final state particles, thus it would be expected that this would have the worst reconstruction efficiency as well. Fig 38, shows the reconstruction efficiencies for the pixel and reference signal for the reconstructable π^+. On these plots, the normalized momentum distributions are shown as well. In both cases, it is clear that the reconstruction efficiency is very low at the points where the momentum distribution is very high, meaning that a lot of the reconstructable π^+ will not be reconstructed. The addition of pixel detectors, together with the material reweighting factor, appears to not have an effect on the reconstruction efficiency in this case in the region of interest, i.e. at the high momentum distribution of the π^+ and also does not appear to effect the overall p_t distribution.

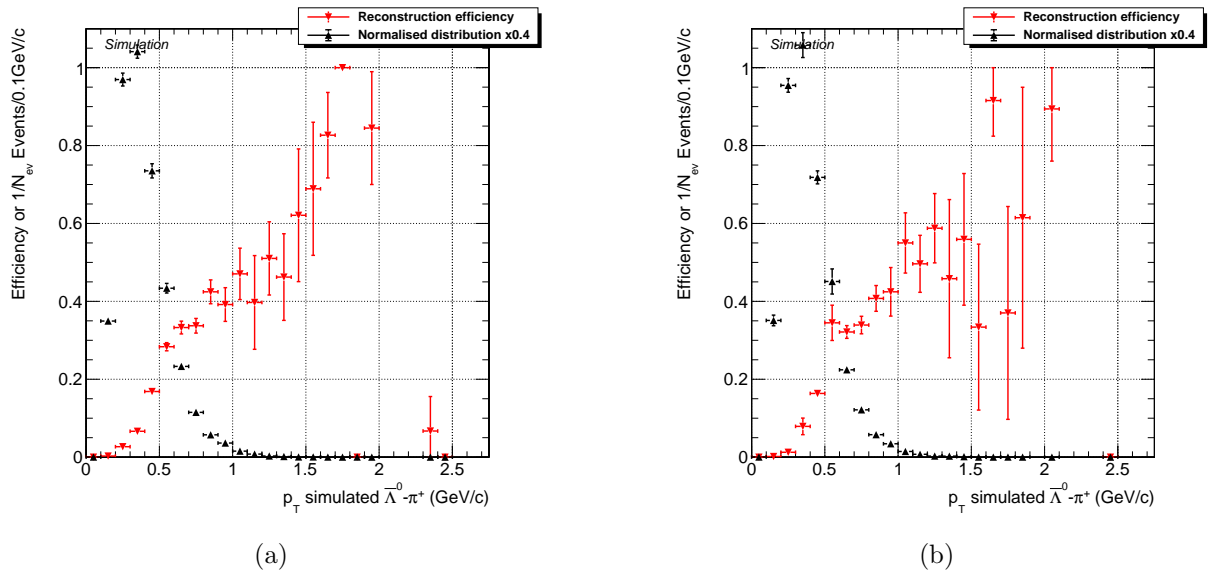(a)   (b)

Figure 38: Reconstruction efficiencies and transverse momentum distributions for the π^+ of the $\bar{\Lambda}^0$ for the reference signal (a) and the pixel signal (b).

Another interesting result is the reconstruction efficiency of the π^+ in function of the η of the $\bar{S}$ particles when comparing the reference and pixel signals. Fig 39 shows these plots. There is a clear difference in reconstruction efficiencies, where the reconstruction efficiency for the pixel signal lies a little lower and has two additional minima present centrally. By adding the possibility for the $\bar{S}$ to interact further in the pixel detector, the π^+ particle could travel through fewer detector layers, causing the observed decrease in the reconstruction efficiency.

(a)   (b)
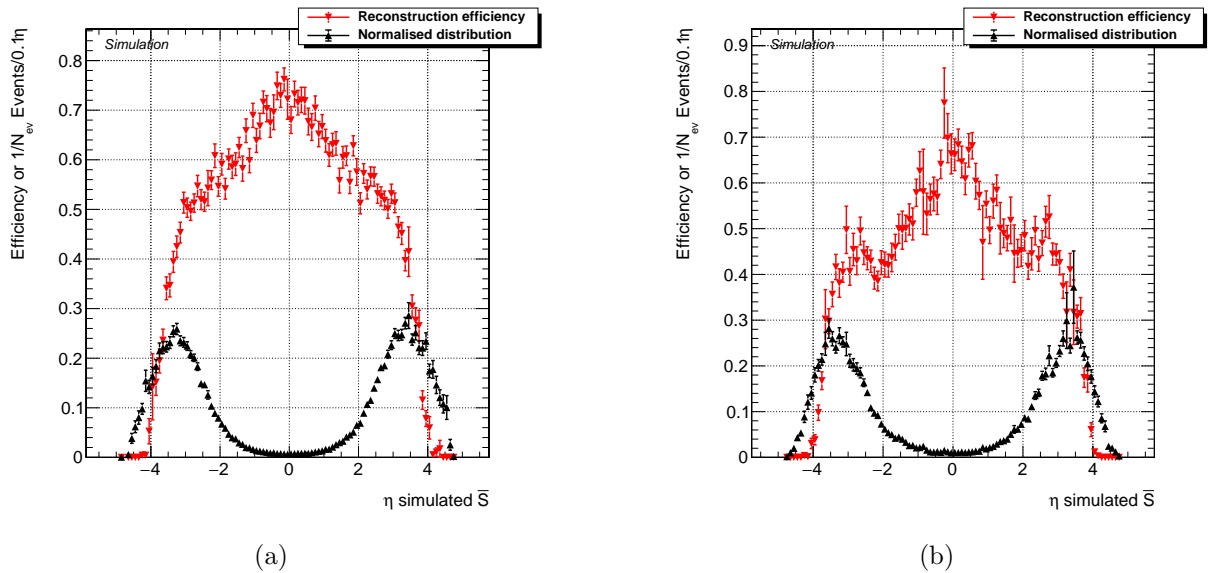
Figure 39: Reconstruction efficiencies in function of the η of the $\bar{S}$ for the π^+ of the $\bar{\Lambda}^0$ for the reference signal (a) and the pixel signal (b).

This effect can be further illustrated in the reconstruction efficiencies for the $\bar{p}$ in function of the transverse displacement of its creation vertex. These are shown in Fig 40. When looking

at the normalized distributions of the transverse displacements, it can be lightly seen that for the pixel signal, the distribution lies a little bit above that of the reference for higher values. From the reconstruction efficiencies, information about the CMS detector itself can be extracted. The reconstruction efficiencies fall steeply at a value of about $l_0(bs) \approx 65cm$. This is due to the layout of the detector. The last layer used for tracking the seeds sits at a radius of about $l_0(bs) \approx 70cm$, meaning that the final state particles created at transverse displacement of about 65 cm, will be difficult to reconstruct. The reconstruction efficiencies are similar for reference and pixel signal as is expected as this should have no influence on them.
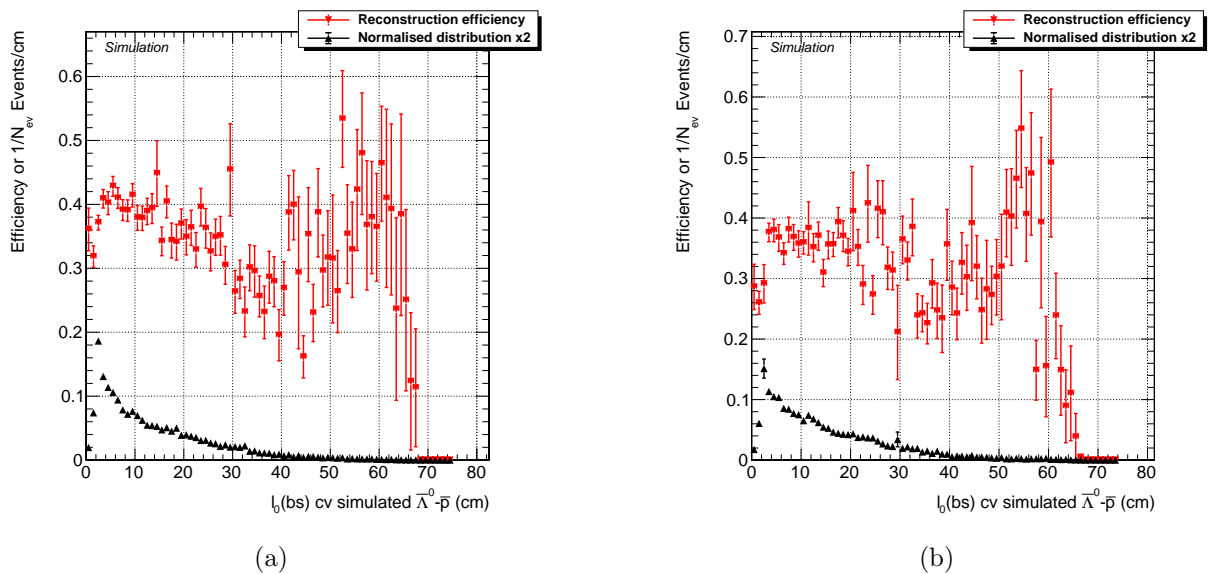

Figure 40: Reconstruction efficiencies in function of the transverse displacement for the π^+ of the $\bar{\Lambda}^0$ for the reference signal (a) and the pixel signal (b).

The main goal of this section is to study the reconstruction efficiencies for the $\bar{S}$ particle itself. These are given in function of η, the longitudinal interaction vertex displacement and the transverse momentum of the $\bar{S}$ in Fig 41, 42, 43. On these plots, the low statistics involved can clearly be seen by the big error bars and the low binnings. The reconstruction efficiencies in function of its η show that it is highest at the points where the distribution is at its lowest, i.e. centrally. This is also true for the transverse momentum. The $\bar{S}$ has a low transverse momentum and at that region, the reconstruction efficiencies can be seen to be very low. When comparing pixel and reference signals, the reconstruction efficiencies in function of the kinematic variables appear to be very similar. However, in general for the pixel signal the total reconstruction efficiency lies a little lower as can be seen from comparing Table 2 with Table 3. These tables show the overall reconstruction efficiencies of all the particles involved in the search signal for reference and pixel signal, respectively.

From both tables, it is obvious that the reconstruction efficiencies of the $\bar{S}$ are very low, with percentages of 0.0020% and 0.0017% for the reference and pixel signal, respectively. This means that even though a very large data set would be used for the search, such as in [2], only a very small fraction of interacting $\bar{S}$ particles can be reconstructed and selected. However, Although the reconstruction efficiency of the pixel signal is lower than that of the reference, which was expected as explained in section 17, there is still an extra amount of nuclear interaction length

expected by adding the pixel detectors. This is expected to be of order $\mathcal{O}(10)$. Looking back at Eq 10, if the reconstruction efficiency of the $\bar{S}$ only differ by 0.0003% but a larger amount of events will be available due to the extra presence of the pixel detector, a better upper limit can be placed on the cross-section of the $\bar{S}$ production cross-section multiplied by the cross-section for the $\bar{S}$ annihilation with a neutron that results in $K^0_{\bar{S}}$ and a $\bar{\Lambda}^0$.
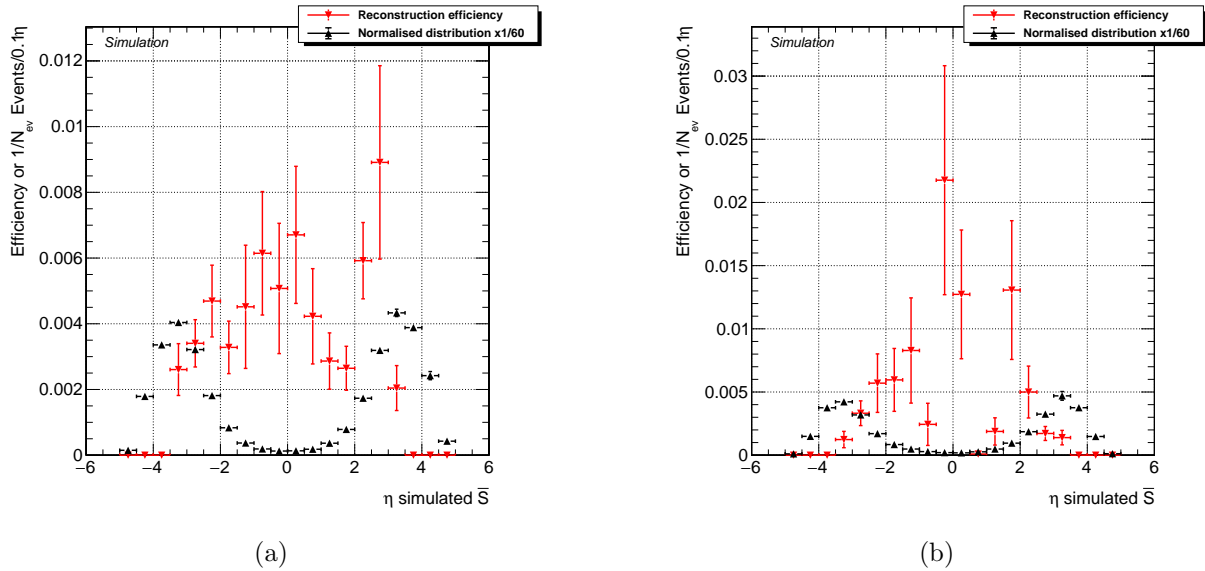

Figure 41: Reconstruction efficiencies of the $\bar{S}$ in function of its η for pixel signal (b) and reference signal (a).
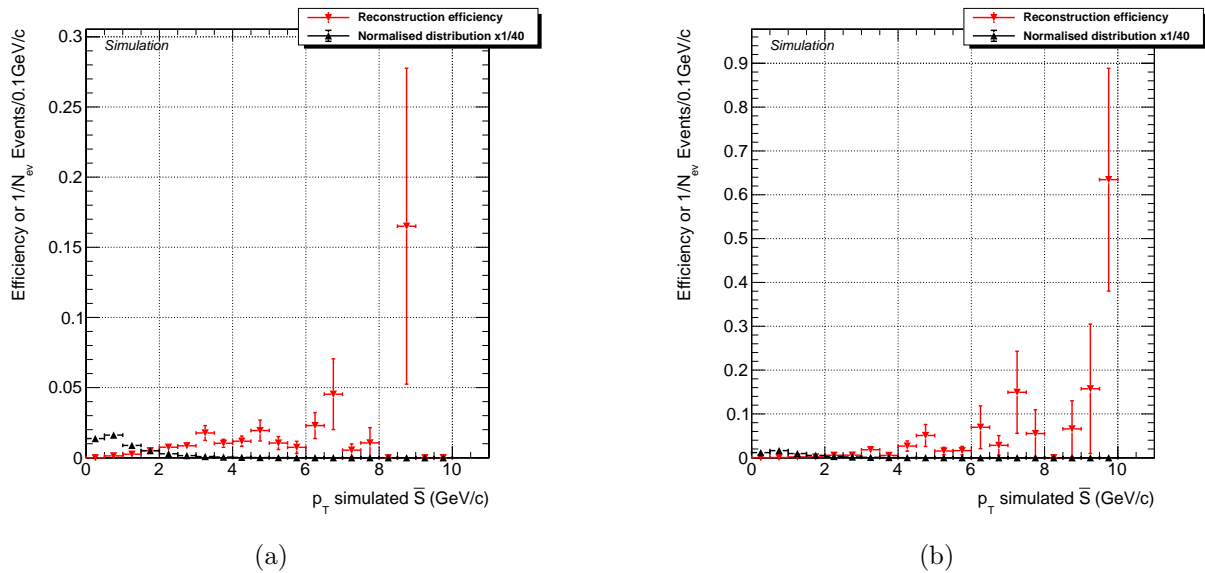
Figure 42: Reconstruction efficiencies of the $\bar{S}$ in function of its transverse momentum for the pixel signal (b) and reference signal (a).

(a)   (b)
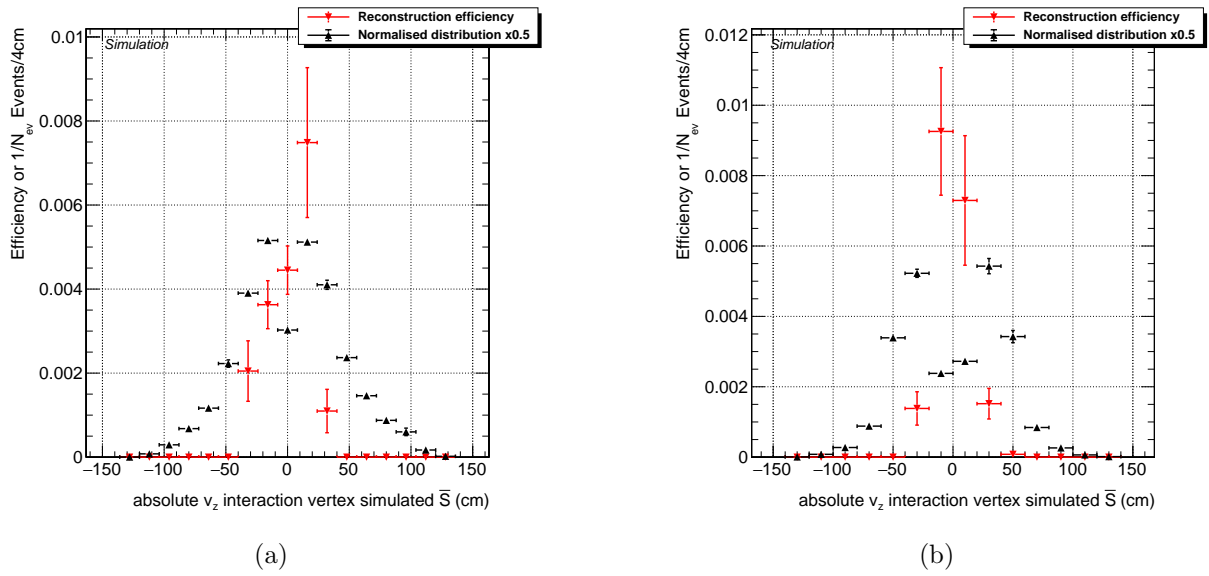
Figure 43: Reconstruction efficiencies of the $\bar{S}$ in function of its longitudinal displacement for pixel signal (b) and reference signal (a).

$\bar{S}$ reconstructability	0.75 %
$\bar{\Lambda}^0$-π^+ reconstruction efficiency in reconstructable events	12.8 %
$\bar{\Lambda}^0$-$\bar{p}$ reconstruction efficiency in reconstructable events	37.2 %.
$K^0_{\bar{S}}$-π^+ reconstruction efficiency in reconstructable events	29.1 %
$K^0_{\bar{S}}$-π^- reconstruction efficiency in reconstructable events	30.0%
Λ^0 reconstruction efficiency in reconstructable events	3.1%
$K^0_{\bar{S}}$ reconstruction efficiency in reconstructable events	6.4%
$\bar{S}$ reconstruction efficiency in reconstructable events	0.27%
Overall $\bar{S}$ reconstruction efficiency (ϵ_{reco})	0.0020%

Table 2: Reconstruction efficiencies of all the particles in the search signal for the *reference* signal.

$\bar{S}$ reconstructability	0.75 %
$\bar{\Lambda}^0$-π^+ reconstruction efficiency in reconstructable events	13.4 %
$\bar{\Lambda}^0$-$\bar{p}$ reconstruction efficiency in reconstructable events	34.3 %.
$K_{\bar{S}}^0$-π^+ reconstruction efficiency in reconstructable events	25.5 %
$K_{\bar{S}}^0$-π^- reconstruction efficiency in reconstructable events	25.6%
$\bar{\Lambda}^0$ reconstruction efficiency in reconstructable events	2.9%
$K_{\bar{S}}^0$ reconstruction efficiency in reconstructable events	4.5%
$\bar{S}$ reconstruction efficiency in reconstructable events	0.23%
Overall $\bar{S}$ reconstruction efficiency (ϵ_{reco})	0.0017%

Table 3: Reconstruction efficiencies of all the particles in the search signal for the *pixel* signal.

7   Signal selection and backgound suppression

A signal in particle physics is a specific process of interest for the analysis made. In this thesis, the signal of interest is given by Eq 10. However, it is possible that other processes that are not of particular interest in the analysis actually look like the desired process and thus would leave similar signatures in the CMS detector. These similar processes are known as *background* signals. In the study of a signal, it is thus of crucial importance that the so-called signal-to-background ratio is increased. This signal-to-background ratio can be increased by making some selection cuts in the data.

In [2], a detailed study of the background rejection was done with the use of reconstructed S candidates, instead of $\bar{S}$. This is because the S candidates do not annihilate on neutron and can thus be used as a background control sample. It was then shown that the background is due to random combinations of $K_{\bar{S}}^0$ and $\bar{\Lambda}^0$. Background cuts were applied in this study to suppress the background. The cuts were made with the use of a boosted decision tree (BDT). This is a machine-learning technique that is used in regression and classification tasks.
The use of a BDT falls outside the scope of this thesis. In this section, we will make use of a tighter version of the preselection cuts made in [2] to see the number of $\bar{S}$ candidates that survive these cuts, to give us an intuition of the signal and background selection efficiency. Before applying these cuts, a *genmatching* condition has to be made on the reconstructed $\bar{S}$ events. This condition is chosen to be $\Delta L_{xyz,iv} < 0.5\ cm$, i.e. that the distance between the interaction vertices simulated and reconstructed particles is less than 0.5 *cm*. A small difference in one of the cuts is made for the pixel signal. All the cuts made for the background suppression here are shown in Table 4. The different cut is given in the second cell, where a cut was made that the transverse displacement of the interaction vertex of the $\bar{S}$ should be between 2.1 cm and 2.3 cm. For the reference signal this was a proper choice as the beampipe was the only place of interaction and thus would have to be between these values. For this reason, the upper requirement on this cut has been removed for the pixel signal.

When performing these cuts on the events in the simulation, 48.2 % and 39.7 % of the events remained for the reference signal and pixel signal, respectively. The cuts thus appear to be harder on the pixel signal. As mentioned, these choice cuts were obtained using a BDT for the reference signal. A further study should be done to analyze the cuts to be made for the pixel

signal using a BDT.

Pixel signal cuts	Reference signal cuts
$|v_{z,iv}| < 28$ cm	$|v_{z,iv}| < 28$ cm
$2.1 < l_{0,bpc,iv}$	$2.1 < l_{0,bpc,iv} < 2.3$
$1.8 < \Delta\phi_{\bar{\Lambda},K_{\bar{S}}^0}$	$1.8 < \Delta\phi_{\bar{\Lambda},K_{\bar{S}}^0}$
$|\Delta\eta_{\bar{\Lambda},K_{\bar{S}}^0}| < 1.5$	$|\Delta\eta_{\bar{\Lambda},K_{\bar{S}}^0}| < 1.5$
$0.5 < openingsangle_{(\bar{\Lambda},K_{\bar{S}}^0)} < 1.3$	$0.5 < openingsangle_{(\bar{\Lambda},K_{\bar{S}}^0)} < 1.3.$
$0.1 < openingsangle_{(\bar{S},K_{\bar{S}}^0)} < 1.4$	$0.1 < openingsangle_{(\bar{S},K_{\bar{S}}^0)} < 1.4$
$0.1 < openingsangle_{(\bar{S},\bar{\Lambda})} < 1.0$	$0.1 < openingsangle_{(\bar{S},\bar{\Lambda})} < 1.0$
$|\eta_{\bar{S}}| < 3.5$	$|\eta_{\bar{S}}| < 3.5$
$|\eta_{K_{\bar{S}}^0}| < 4.0$	$|\eta_{K_{\bar{S}}^0}| < 4.0$
$d_0/l_{0,bs} < 0.2$	$d_0/l_{0,bs} < 0.2$
$|min\ d_{z,bs,\bar{S}}| < 4$	$|min\ d_{z,bs,\bar{S}}| < 4$
$|p_{t,K_{\bar{S}}^0}| < 1.2$	$|p_{t,K_{\bar{S}}^0}| < 1.2$
$0 < m_{\bar{S}} < 4$	$0 < m_{\bar{S}} < 4$

Table 4: All the background cuts made to give an intuition of the background efficiency ($\epsilon_{BckCuts}$) on the reference signal vs. pixel signal.

8 Conclusion

The sexaquark is a proposed theoretical particle by G. Farrar, and consists of a strongly bound state of six quarks. It was suggested that the particle could be a dark matter candidate if its mass is in the right range. It is possible that the particle could be produced in proton-proton collisions in hadron colliders. The LHC is a very interesting opportunity to study this particle due to its high luminosity and the fact that the production rate of the $\bar{S}$ would be low.

In [2], J. De Clerq performed a first-ever search for the sexaquark at the LHC using the following search channel:

$$\bar{S} + n(udd) \rightarrow \bar{\Lambda}(\bar{u}\bar{d}\bar{s}) + \mathrm{K}_S^0(\frac{d\bar{s} - \bar{d}s}{2})$$
$$\bar{\Lambda}(\bar{u}\bar{d}\bar{s}) \rightarrow \bar{p}\ (\bar{u}\bar{u}\bar{d}) + \pi^+(u\bar{d}) \tag{17}$$
$$\mathrm{K}_S^0(\frac{d\bar{s} - \bar{d}s}{2}) \rightarrow \pi^+(u\bar{d}) + \pi^-(\bar{u}d)$$

.

In the study of [2], an upper limit was placed on the cross-section of the S production cross-section multiplied by the cross-section for the S annihilation with a neutron that results in $K_{\bar{S}}^0$ and a $\bar{\Lambda}^0$. This was done by making a full analysis of the reconstruction efficiencies in a signal simulation, background rejections, and systematic uncertainties. In the signal simulation in the study, only the beampipe of the CMS was added as material in which the $\bar{S}$ particle of the signal could interact. However, it was mentioned that the addition of extra material could increase the strength of the upper limit as the nuclear interaction length of the $\bar{S}$ should increase by an order of $\mathcal{O}(10)$.

In this thesis, a study was performed to evaluate the reconstruction efficiencies when additional pixel detector material was added to the simulation. A choice was made to add the first four inner tracking detector layers to the simulation, as it might be possible that the reconstruction efficiencies in the layers behind those would be low due to the fact that there are fewer tracking detectors behind to detect the daughter and granddaughter particles of the $\bar{S}$. This reconstruction efficiency, as well as the kinematic variables in the simulation and background cuts, was made for a signal with the pixel detectors included and for a signal where again only the beampipe was present, such that a comparison could be properly made.

Adding the pixel detectors to the signal simulation required a so-called material reweighting factor due to the killing loop present in the simulation software for the $\bar{S}$. This reweighting factor was a new concept that had to be introduced in this thesis for a further correct signal simulation. This reweighting and the addition of the pixel detector had many effects on kinematic variables and the interaction/creation vertices of the particles involved in the search signal.

Analysis of the reconstruction efficiencies showed that the overall reconstruction efficiency is very low for the reference and pixel signal and was found to be $\epsilon_{reco} = 0.0020\%$ and $\epsilon_{reco} = 0.0017\%$, respectively. Thus the pixel reconstruction efficiency is about 0.0003% lower. This low reconstruction efficiency can be explained due to the fact that the final state particle do not necessarily point toward the luminous region and because the final state particles have a very low p_t. The small difference in reconstruction efficiency for pixel and reference was an expected result as the interactions of the $\bar{S}$ happening in the pixel layers would have been less efficient

to reconstruct due to fewer tracker layers being available afterward for the daughter particles as well as the fact that the daughter particles could also have a larger impact parameter.

Finally, performing background suppression cuts, which were chosen based on the BDT in [2], showed that 48.2% of the events survived the cuts for the reference signal, and 39.7% survived it in the pixel signal. These cuts give us an intuition of the background cuts efficiency $\epsilon_{BckCuts}$, but a more detailed analysis should be made for this in the pixel signal.

The reconstruction efficiency and background cuts efficiency of the pixel signal is lower compared to the reference signal. The product of both efficiencies gives an efficiency of 0.000964% and 0.000675% for the reference and pixel signal, respectively. Thus the pixel-over-reference ratio for the efficiencies is ≈ 0.699. This means that if the number of events does indeed increase by an order of $\mathcal{O}(10)$, which is heavily suggested by the weight factor distribution of Fig 11, the upper limit found in [2] could be scaled a factor in the range of 1-$\mathcal{O}(10)$. Thus a dedicated analysis involving the pixel detectors in the signal simulations could provide a higher upper limit on the $\bar{S}$ production cross-section ($\sigma(\text{pp} \rightarrow \bar{S})$) times the cross-section for the $\bar{S}$ annihilation with a neutron that results in a K_S^0 $\bar{S}$ and a $\bar{\Lambda}^0$.

9 Outlook

The influence of the addition of pixel layers in the signal simulation on the efficiencies has been well established in this thesis. However, this search channel at the LHC for the Sexaquark is not fully optimized.

While it appears that the inclusion of the pixel layers would provide a better upper limit found in [2], actual investigation of the increase of the number of events when pixel layers are added should still be done to find a more exact estimate of the factor with which the upper limit is increased. Due to an unfortunate lack of time, this was not done in this thesis.

As was already mentioned, all the computations made in the signal simulations were done with the Fermi motion for Beryllium in all the material in the CMS detector. This is certainly not the case and while a comparison was made for kinematic variables in the signal simulation with Fermi motions of two different elements, more detailed research has to be done in this region to study the possible effects of the different Fermi motions.

In this thesis, an estimate for the background cuts efficiency was performed using the background suppression cuts given in [2]. These cuts were decided with the use of a BDT and were made in the case of a reference signal. A further study of the background suppression cuts could be made in the case of a pixel signal as well as using a BDT to get a better understanding of background cuts efficiency when compared to that of the reference signal.

The focus of this research was to study to influence of the additional pixel layers in the signal simulations and thus study the influence of it on the actual upper limit in [2]. However, there could still be other ways to optimize the search strategy made here. An example of this could be a dedicated tracking algorithm for low momentum tracks with high displacement such that the reconstruction efficiencies in the signal simulation could be increased.

References

[1] Glennys R. Farrar, Stable Sexaquark, arXiv:1708.08951v1[hep-ph]

[2] De Clercq, Jarne Theo. The Upgraded Outer Tracker for the CMS Detector at the High Luminosity LHC, and Search for Composite Standard Model Dark Matter with CMS at the LHC. Diss. Vrije U., Brussels, 2020.

[3] Bertone, G., D. Hooper, and J. Silk. "Particle dark matter: Evidence, candidates and constraints, Phys." arXiv preprint hep-ph/0404175 405 (2005): 279.

[4] K. G. Begeman, A. H. Broeils and R. H. Sanders, 1991, MNRAS, 249, 523

[5] F. Zwicky. "On the Masses of Nebulae and of Clusters of Nebulae". In: apj 86 (1937), p. 217. DOI: 10.1086/143864.

[6] D. Clowe, M. Bradac, A. H. Gonzalez, M. Markevitch, S. W. Randall, C. Jones, D. Zaritsky, A direct empirical proof of the existence of dark matter, Astrophys. J. Lett., 648 (2006) L109–L113. arXiv:astro-ph/0608407, doi:10.1086/508162.

[7] M. Tanabashi et al. "Review of Particle Physics". In: Phys. Rev. D 98 (3 2018),

[8] Perkins, Donald H. Particle astrophysics. No. 10. Oxford University Press, 2009. p. 030001. DOI: 10.1103/PhysRevD.98.030001.

[9] Planck Collaboration. "Planck 2018 results. VI. Cosmological parameters". In: arXiv e-prints (2018). arXiv: 1807.06209 [astro-ph.CO].

[10] E. Mobs. The CERN accelerator complex. URL: https : / / cds . cern . ch / record / 2197559.

[11] https://cms.cern/news/cms-detector-design

[12] Adam, Wolfgang, et al. "The CMS Phase-1 pixel detector upgrade." Journal of Instrumentation 16.02 (2021): P02027.

[13] CMS collaboration. (2014). Description and performance of track and primary-vertex reconstruction with the CMS tracker. Journal of Instrumentation, 9(10), P10009.

[14] Bauer, Julia. "Prospects for the Observation of Electroweak Top Quark Production with the CMS Experiment, KIT, Karlsruhe." Dept. Phys (2010).

[15] Belle Collaboration. "Observation of a Narrow Charmoniumlike State in Exclusive B $\pm \rightarrow$ K $\pm$ + J/ Decays". In: Phys. Rev. Lett. 91 (26 2003), p. 262001. DOI: 10.1103/PhysRevLett.91.262001.

[16] LHCb Collaboration. "Observation of J/p Resonances Consistent with Pentaquark States in 0 b $\rightarrow$ J/K p Decays". In: Phys. Rev. Lett. 115 (2015), p. 072001. DOI: 10.1103/PhysRevLett.115.072001. arXiv: 1507.03414 [hep-ex].

[17] R. L. Jaffe, Perhaps a Stable Dihyperon, Phys. Rev. Lett. 38, 195 (1977); Erratum Phys. Rev. Lett. 38, 617 (1977)

[18]] J. K. Ahn et al., Production of 4H Hypernuclei, Phys. Rev. Lett. 87, 132504 (2001)

[19]] J. Badier et al., Mass and lifetime limits on new long-lived particles in 300 GeV/c = interactions, (NA3), Z. Phys. C31, 21 (1986).

[20]] R. H. Bernstein et al., Search for new, long-lived, neutral particles, Phys. Rev. D37, 3103 (1988).

[21] J. Belz et al. , Search for the Weak Decay of an H Dibaryon, (BNL-E888) Phys. Rev. Lett. 76, 3277 (1996), [Phys. Rev.C56,1164(1997)], arXiv:hep-ex/9603002[hep-ex].

[22] A. Alavi-Harati et al. (KTeV), Search for the Weak Decay of a Lightly Bound H Dibaryon, Phys. Rev. Lett. 84, 2593 (2000), arXiv:hep-ex/9910030[hep-ex].

[23] H. Takahashi et al., Phys. Rev. Lett. 87, 212502 (2001)

[24] B. H. Kim et al. (Belle), Phys. Rev. Lett. 110, 222002 (2013), arXiv:1302.4028 [hep-ex].

[25] S. A. Yost and C. R. Nappi. "Mass of the H dibaryon in a chiral model". In: Phys. Rev. D 32 (3 1985), pp. 816–818. DOI: 10.1103/PhysRevD.32.816.

[26] K.F. Liu and C.W. Wong. "MIT bag model with center-of-mass correction". In: Physics Letters B 113.1 (1982), pp. 1 –5. ISSN: 0370-2693. DOI: 10 . 1016 / 0370 - 2693(82)90096-X

[27] E. W. Kolb and M. S. Turner. "Dibaryons cannot be the dark matter". In: Phys. Rev.

[28] G. R. Farrar. "A precision test of the nature of Dark Matter and a probe of the QCD phase transition". In: arXiv e-prints (2018). arXiv: 1805.03723 [hep-ph].

[29] Navarro, J. F., Frenk, C. S., White, S. D. M. 1997, ApJ, 490, 493, doi: 10.1086/304888

[30] Moore, B., Governato, F., Quinn, T., Stadel, J., Lake, G. 1998, ApJL, 499, L5, doi: 10.1086/311333 283, L72, doi: 10.1093/mnras/283.3.L72

[31] Carignan, C., Beaulieu, S. 1989, ApJ, 347, 760, doi: 10.1086/168167

[32] Lake, G., Schommer, R. A., van Gorkom, J. H. 1990, AJ, 99, 547, doi: 10.1086/115349 D 99."arXiv:1809.06003" (6 2019), p. 063519. DOI: 10.1103/PhysRevD.99.063519.

[33] BaBar Collaboration. "Search for a Stable Six-Quark State at BABAR". In: Phys. Rev. Lett. 122 (7 2019), p. 072002. DOI: 10.1103/PhysRevLett.122.072002.

[34]] J. Beringer et al. (2012): Particle listings K0 L, Available at: http://pdg.lbl.gov/2012/listings/rpp2012-list-K-zero-L.pdf

[35] Torbjorn Sjostrand et al., A Brief Introduction to PYTHIA 8.1, Comput.Phys.Commun. 178 (2008) 852-867, arXiv:0710.3820

[36] Pierog, T., Karpenko, I., Katzy, J., Yatsenko, E., Werner, K. (2019). EPOS LHC: test of collective hadronization with LHC data (2013). arXiv preprint arXiv:1306.0121.

[37]] S. Agostinelli et al., GEANT4: A simulation Toolkit, Nucl.Instrum.Meth A506 (2003) 250- 303

[38]] J. Allison et al., Geant4 developments and applications, IEEE Transactions on Nuclear Science 53 No. 1 (2006) 270-278

[39] J. Allison et al., Recent developments in GEANT4, Research Nucl.Instrum.Meth A 835 (2016) 186-225

[40] Tracker Group of the CMS Collaboration. (2020). The CMS Phase-1 pixel detector upgrade. arXiv preprint arXiv:2012.14304.

[41] Ryckebusch, J., Cosyn, W., Stevens, S., Casert, C., Nys, J. (2019). The isospin and neutron-to-proton excess dependence of short-range correlations. Physics Letters B, 792, 21-28.